ELSEVIER

Contents lists available at ScienceDirect

Additive Manufacturing

journal homepage: www.elsevier.com/locate/addma



Tuning α precipitation via post-heat treatments in direct energy deposited metastable β Ti-5Al-5Mo-5V-3Cr alloy and its impact on mechanical properties

Dian Li^a, Sydney Fields^a, Xing Zhang^{b,c}, Deepak V Pillai^a, Mohammad Merajul Haque^b, Tirthesh Ingale^a, Vishal Soni^a, Yiliang Liao^{b,*}, Rajarshi Banerjee^a, Yufeng Zheng^{a,*}

ARTICLE INFO

Keywords: Direct energy deposition Post-heat treatment Titanium alloys Phase transformation Mechanical behavior

ABSTRACT

In this study, the strength and ductility of a direct energy deposited (DEDed) metastable β Ti-5Al-5Mo-5 V-3Cr (wt%, Ti-5553) alloy was explored by tuning the formation of various α microstructures through post-heat treatments. The microstructure of DEDed Ti-5553 with and without post-heat treatments was systematically studied using scanning electron microscopy, three-dimensional (3D) focused ion beam-scanning electron microscopy tomography, transmission electron microscopy, scanning transmission electron microscopy, and atom probe tomography. Nanoscale ω phase and O' phase particles were observed in the as-built DEDed Ti-5553 without post-heat treatment for the first time. By altering the aging temperatures and heating rates during post-heat treatments, various microstructural evolution pathways were activated, leading to α microstructures with different sizescales, morphologies, and number densities. By fast heating and isothermal aging at 600°C for 2 hours, refined α microstructure was formed through the pseudospinodal decomposition mechanism. While slow heating (at the heating rates of 5 °C/min or 0.5 °C/min) to 600°C and isothermal aging for 2 hours, super-refined α microstructures were produced respectively, primarily via ω -assisted and O'-assisted α precipitation mechanisms. By fast heating to and isothermal aging at 700°C, fine-scaled intragranular α microstructure was formed, dramatically different in morphology and sizescale from the coarse a microstructure formed in the casted Ti-5553, which is suspected to be related to the indirect influence of nanoscale isothermal ω phase particles formed during the DED process and the excess oxygen introduced during the DED process. With fast heating to and isothermal aging at 800°C, coarse α microstructure forms through the classical nucleation and growth mechanism. Various α microstructures led to a drastic change of mechanical properties with improvements up to a 55 % increase in hardness and 92 % increase in tensile yield strength, compared with as-built DEDed Ti-5553. Our work indicates the feasibility of achieving tailored mechanical properties in DEDed metastable β -Ti alloys by tuning α microstructures through selectively activating various phase transformation mechanisms via post-heat treatments.

1. Introduction

In recent years, the growing demand for aerospace applications highlights the significance of metastable β titanium (β -Ti) alloys, due to their outstanding hardenability, excellent fracture toughness, and great resistance to fatigue [1–3]. For example, Ti-5Al-5Mo-5 V-3Cr (wt%, Ti-5553) has found successful applications in aircraft structural components like airframes and landing gear in Boeing 787 and Airbus 380

aircraft due to its impressive tensile strength up to 1400 MPa, fracture toughness up to $80MPa \bullet \sqrt{m}$, and run-out stress at 10^7 cycles of 758 MPa, significantly higher than those of Ti-6Al-4 V (wt%, Ti-64) [4]. However, conventional manufacturing of large-scale metastable β -Ti components remains challenging due to their poor machinability and limited forging range [5]. To address these challenges, additive manufacturing (AM) techniques, such as direct energy deposition (DED), have emerged as effective methods for producing near-net-shape

E-mail addresses: leonl@iastate.edu (Y. Liao), yufeng.zheng@unt.edu (Y. Zheng).

^a Department of Materials Science and Engineering, University of North Texas, Denton, TX 76203, USA

^b Department of Industrial & Manufacturing Systems Engineering, Iowa State University, Ames, IA 50011, USA

^c School of Mechanical and Electrical Engineering, Soochow University, Suzhou, Jiangsu 215100, China

^{*} Corresponding authors.

Ti-based components, which can significantly reduce material waste and production time associated with conventional machining processes [6–8]. Additionally, the design flexibility of AM makes it an attractive choice for manufacturing Ti-based components with complex geometry [9].

Up to date, the research on AM of Ti alloys has primarily focused on widely used α/β titanium alloys such as Ti-64 [10–15]. Limited efforts have been dedicated to studying AM of metastable β -Ti alloys. One of the significant drawbacks of AM that is characteristic and prevalent in titanium alloys is the formation of coarse and columnar β -Ti grains that form as a result of the unique thermal cycling process in both DED and laser powder bed fusion (LPBF) techniques. Primary studies involving LPBF metastable β-Ti alloys primarily investigate the printability to optimize density, decrease porosity and β flecks, and produce crack-free specimens [16-19]. However, due to the coarse columnar grains, mechanical properties are typically anisotropic, which raises concerns about how to successfully meet ASTM standards for industrial implementation. Recent work has centered on employing various pre-, in-situ, and post-printing methods to achieve equiaxed β grains and α microstructures with different sizescales, aiming to enhance the mechanical performance in LPBF metastable β-Ti alloys [20–22]. Liu et al. added different β -stabilizing elements including Fe, Co, Mo to metastable β Ti-xFe-yCo-1Mo (wt%) alloy to achieve a fully equiaxed β grain microstructure and a combination of $\sim \! 1200$ MPa tensile strength and $\sim \! 12$ % ductility [20]. Schwab et al. utilized the strategy of substrate heating in LPBF of Ti-5553 to achieve the finely distributed α microstructure in the β matrix and a combination of $\sim \! 1000 \text{ MPa}$ compressive strength and 20 % true compressive strain [21]. Carlton et al. reported that \sim 1000 MPa tensile strength and \sim 10 % ductility in LPBF Ti-5553 can be achieved after post-heat treatment at 700°C [22]. However, these studies mainly focus on microscale phases, such as β grains and α precipitates. The potential influence of various nanoscale phases that can form during the AM process on the microstructure evolution and mechanical properties of AMed metastable β-Ti alloys remains largely unknown.

While initial studies have investigated the printability of Ti-5553 by DED with an emphasis on the optimization towards printing of crackfree specimens [16,17], there are limited studies regarding the microstructure and mechanical properties of DEDed Ti-5553 [18,19]. Previous studies also focused on applying aging techniques, notably duplex aging and its influence on strength and ductility [18,19,23]. Studies revealed that the DEDed Ti-5553 specimens displayed a microstructure consisting of supersaturated β grains, resulting in decent ductility (approximately 13.3 % uniform elongation) but a relatively low ultimate tensile strength (yield strength ~780 MPa) [18,19]. This level of strength cannot satisfy the requirements for a variety of aerospace applications. To enhance the strength of DEDed Ti-5553, which consists of predominately β grains with body-centered cubic (bcc) structure, subsequent post-heat treatment is typically employed to induce the formation of α precipitates with hexagonal closed-packed (hcp) structure through precipitation hardening [18,19]. Recent studies have indicated that a variety of non-conventional phase transformation mechanisms can be activated to form different fine-scaled α microstructures with different sizes, morphologies, and number densities in metastable β -Ti alloys via the accurate control of heat treatment conditions (heating rate, aging temperature, and duration) [24-29]. Our previous studies integrating experimental and computational simulation have shown that for Ti-5553, while step-quenching to 600°C from above the β-transus temperature or up-quenching to 600°C from room temperature, the refined α microstructure with a number density of approximately 5 ppts/μm² can be formed by the pseudospinodal decomposition mechanism [24,30]. The large number of local compositional fluctuations in the interior of the β grains will act as favorable nucleation sites for the subsequent precipitation of α phase. The hcp-structured α phase is formed by the rapid displacive mode, and the equilibrium composition reached via long-range diffusion [24,30]. Pseudospinodal

decomposition has been reported in a variety of metastable β - Ti alloys, e.g., Ti-5Al-5Mo-5 V-3Cr-1Zr (Ti-55531, wt%) [31], Ti-15 Nb-3Fe [32], and Ti-12 Nb-5Al-5Mo-3Cr-0.5Fe (wt%) [33]. Additionally various studies have shown that the pre-formed metastable ω phase can assist the following α precipitation and refine the α microstructure [25–27, 29]. For Ti-5553, during slow heating to 600°C (e.g., at a heating rate of 5°C/min), nano-scaled hexagonal structured metastable ω precipitates can be formed in the interior of the β grains [29]. The large number of ω precipitates can change the local compositional field and stress field near the preformed ω/β interface and thus serve as the favorable nucleation sites of so-called super-refined α precipitates (number density ~35 ppts/ μ m²) [29]. Moreover, these findings have been effectively applied to tailor the α microstructure of cast Ti-5553 and other metastable β -Ti alloys to achieve the desired mechanical properties [34,35].

However, compared to cast Ti alloys, DEDed Ti alloys exhibit unique as-printed microstructural features due to the rapid cooling and periodic thermal cycles involved in the AM process. For example, recent studies on DEDed Ti-64 have shown that as-printed parts contain a high density of dislocations caused by the substantial thermal residual stress [36]. These dislocations could affect α precipitation during subsequent post-heat treatment [37,38]. Consequently, there is a critical need to determine the interrelationship between microstructure and mechanical properties in the DEDed metastable β -Ti alloys, particularly, whether non-conventional phase transformation mechanisms, e.g., pseudospinodal decomposition and ω -assisted α precipitation, can be activated in the DEDed Ti-5553. To the best of our knowledge, there has been limited research addressing this question. Sharma et.al., have studied the aging response of DEDed Ti-5553 using a series of sub-transus post-heat treatment and successfully achieve a wide range of yield strength (from 925 MPa to 1371 MPa) and elongation (from 2.0 % to 11.6 %) [19]. Nonetheless, given the complexity of the DED process, further investigation is needed to understand the underlying phase transformation mechanisms for the generation of α microstructures, especially the possible formation of nanoscale structures in the DEDed metastable β -Ti alloys, their roles on the subsequent α precipitation, and the resulting mechanical properties.

In the current work, post-heat treatments of DED-printed Ti-5553 were investigated, with a focus on the formation of various nanoscale phases and α microstructures, and their effects on mechanical properties of AM-fabricated specimens. The microstructure of DEDed Ti-5553 subjected to various post-heat treatments was systematically studied using various electron microscopy techniques, including scanning electron microscopy (SEM), three-dimensional (3D) focused ion beamscanning electron microscopy (FIB-SEM) tomography, transmission electron microscopy (TEM), scanning transmission electron microscopy (STEM), and atom probe tomography (APT). The mechanical properties were measured by hardness, nanoindentation, and tensile tests. Our research effort focuses on the following topics: (1) exploring the nanoscale structure in the DEDed Ti-5553; (2) quantitatively characterizing the microstructure of DEDed Ti-5553 specimens subjected to various post-heat treatments and studying the phase transformation mechanisms responsible for the formation of various α microstructure; (3) determining the interrelationship between the microstructure and mechanical properties (e.g., yield strength and ductility).

2. Material and methods

2.1. DED and post-heat treatment conditions

The Ti-5553 powder used in the DED printing was acquired from AP&C company. The oxygen concentration in the acquired Ti-5553 powders was measured using the LECO ON736 chemical analyzer. Cuboid Ti-5553 samples with dimensions of $20 \times 15 \times 3 \text{ mm}^3$ were additively manufactured on commercially pure (CP)-Ti substrates ($50 \times 30 \times 10 \text{ mm}^3$) using an AMBIT DED/HAAS UMC 750 hybrid system. The DED processing parameters were configured as follows: laser power of

300 W, scanning velocity of 600 mm/min, spot size of 1000 µm, hatch spacing of 750 µm, and layer thickness of 200 µm. The scanning strategy employed a zigzag pattern without interlayer rotations. A combination of these processing parameters was selected since it successfully achieved AM of high-density, crack-free Ti-5553 specimens. The samples were manufactured with dimensions of $40\times15\times5$ mm 3 . All specimens were heat treated below the β transus temperature (T_β , $\sim855^\circ C$) in the MTI GSL-1500X-50-UL tube furnace, being wrapped with CP-Ti foils to minimize oxidization. The as-printed Ti-5553 samples were subjected to two distinct post-heat treatment routes (Fig. 1):

- (1) Different aging temperatures: DEDed Ti-5553 samples in this group were inserted into a furnace preheated, which will be further referred to as up-quenching to 600°C, 700°C, or 800°C respectively, isothermally held for 2 hours, and rapidly quenched in water to room temperature, as depicted in Fig. 1(a).
- (2) Different heating rates: DEDed Ti-5553 samples in this group (Fig. 1(b)) were post-heat treated at different heating rates, specifically 5 °C/min or 0.5 °C/min, to 600°C. Subsequently, they were isothermally held at 600°C for 2 hours before water-quenched to room temperature.

Additionally, one Ti-5553 sample for microstructure comparison was prepared using cast Ti-5553 alloy obtained from TIMET. The cast Ti-5553 sample was $\beta\text{-solutioned}$ at 1000°C for 30 min followed by water quenching, isothermally aged at 700°C for 2 hours, and finally water-quenched to room temperature.

2.2. Materials characterization

DEDed Ti-5553 and post-heat treated Ti-5553 samples were cross-sectioned perpendicular to the laser scanning directions using the Buehler IsoMet High Speed precision saw. The cross-sectioned surfaces were ground and polished following traditional sample preparation routes to a 0.05 μm colloidal silica finish. SEM secondary electron (SE) imaging and backscattered electron (BSE) imaging were conducted using the Thermo Scientific Apreo 2 C SEM at 5 kV. The characterized microstructures were further segmented and quantified using MIPARTM

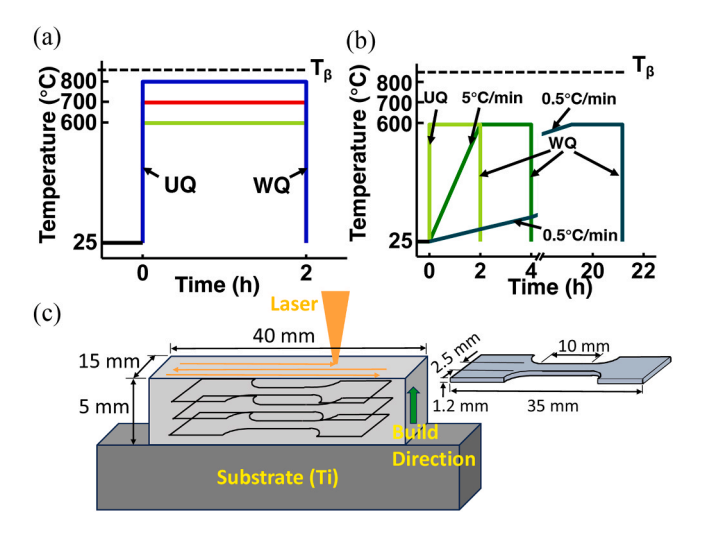


Fig. 1. Schematic diagram showing different post-heat treatment of the DEDed Ti-5553 and dimensions of tensile test samples from DEDed Ti-5553: (a) DEDed Ti-5553 samples up-quenched to 600° C, 700° C, and 800° C respectively, isothermally held for 2 hours, and rapidly quenched into water to room temperature; (b) DEDed Ti-5553 post-heat treated at different heating rates, specifically 5 °C/min and 0.5 °C/min, to 600° C, and isothermally held at 600° C for 2 hours before water-quenched to room temperature; (c) Schematic drawing showing the dimensions and locations of tensile tested samples in the DEDed Ti-5553.

image analysis software [39]. Electron backscattered diffraction (EBSD) data was collected using the embedded EDAX Velocity detector in the Thermo Scientific Apreo 2 C SEM at 20 kV. Site specific thin lamellae for TEM analysis were prepared from the center of β grains using the Thermo Scientific Scios 2 dual-beam focused ion beam/scanning electron microscope (DB FIB/SEM) equipped with an Omniprobe lift-out system. Selected area diffraction pattern (SADP), dark-field (DF) imaging, high angle annular dark-field - scanning transmission electron microscopy (HAADF-STEM) imaging, and X-ray energy dispersive spectroscopy (EDS) were performed using the FEI Talos F200S scanning transmission electron microscope (STEM) equipped with SuperX EDS operating at 200 kV. 3D FIB-SEM tomography was carried out using Thermo Scientific Scios 2 DB FIB/SEM. Automated FIB serial sectioning was conducted using FEI Autoslice 3.14 software, with each slice of 10 nm in thickness milled at 30 kV, and corresponding BSE image recorded at 10 kV. Phase segmentation and 3D reconstruction from 1100 BSE images were performed using MIPARTM image analysis software. For composition analysis on the DEDed Ti5553, atom probe needles were prepared using the FEI Nova 200 NanoLab. These needles were analyzed using the CAMECA local electrode atom probe (LEAP) 5000X system, using the laser mode at a temperature of 50 K, with a detection rate up to 0.7 %, laser pulse energy of 65pJ, and laser pulse frequency of 333 Hz. Additionally, the oxygen concentration change in Ti-5553 during the DED process was evaluated using the LECO ON736 chemical analyzer.

2.3. Mechanical testing

Vickers hardness tests were conducted in five different regions on the cross-section surfaces of DEDed samples at a load of 0.5 N for 20 s using a Wilson Tukon 1202 Vickers hardness tester. Nanoindentation was carried out in at least four different regions in these samples using a KLA Inc. iMicro nanoindenter at a 50 mN load. Tensile tests were performed at room temperature using an Instron 8801 Universal Testing Machine system. To better suit our DED printing system and tensile testing facilities, the miniature specimens were printed with the length of 35 mm and the gauge dimensions of $2.5 \times 1.2 \times 10 \text{ mm}^3$ with the gauge length parallel to the laser scanning direction, as shown in Fig. 1(c). Similar miniature specimens have been used in previous studies, as reported in literature [40-43]. It has been shown that modifying the dimensions of tensile test specimen does not affect the stress-strain response [40-43]. Specifically, critical information relevant to plastic deformation—such as vield strength, ultimate tensile strength and total elongation at fracturemeasured from miniature specimens is comparable to that obtained from standard samples. This was confirmed by our own experiments using the control sample (as-printed, without post-heat treatment) with the dimensions of $6.25 \times 3 \times 25 \text{ mm}^3$. The slimness ratio (k) of our specimens was k = 5.77, which is similar to values reported in literature [44–46]. Tensile force was applied at a strain rate of 10^{-4} /s. Three tensile specimens were tested for each condition. The fracture analysis on the deformed surfaces was performed using a Thermo Scientific Apreo 2 C SEM at 5 kV.

3. Results

3.1. Ti-5553 feedstock powder

The size and morphology of the Ti-5553 powders employed for DED processing were initially characterized using SEM SE imaging and quantitatively analyzed using the MIPARTM image analysis software, shown in Fig. 2(a-c). It was observed in the SEM SE image and MIPAR processed image (Fig. 2(a-b)) that the Ti-5553 powders exhibit a spherical morphology with an aspect ratio 1.08 ± 0.08 . The average diameter of the Ti-5553 powders is approximately $56.8 \mu m$, with more than 95 % of the power particles ranging from 40 μm to $100 \mu m$ in diameter, shown in the powder size distribution histogram in Fig. 2(c).

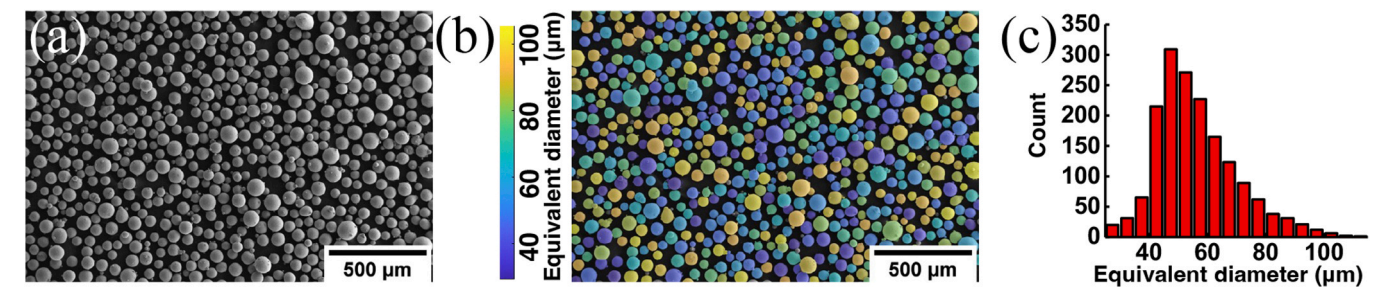


Fig. 2. SEM imaging and MIPAR quantification of Ti-5553 powders used for DED: (a) SEM SE image of Ti-5553 powders; (b) corresponding MIPAR processed image of (a) showing equivalent diameter of Ti-5553 powders; (c) histogram of Ti-5553 powder size showing the distribution of powder equivalent diameter.

The diameter of Ti-5553 powders used in this research is 45–106 μm (with D5 = 45 μm and D95 = 106 μm). Additionally, the oxygen concentration in the acquired Ti-5553 powders measured using LECO ON736 chemical analyzer is approximately 0.0737 \pm 0.0012 wt%. Thus, the above experimental characterization has verified that the spherical Ti-5553 powders with a particle diameter of approximately 40–100 μm and oxygen concentration of 0.0737 wt% were used in the present study.

3.2. Microstructure in DEDed Ti-5553

The grain structure in the DEDed Ti-5553 was analyzed in the crosssection perpendicular to the scanning direction using SEM BSE imaging and EBSD technique, as illustrated in Fig. 3(a-c). Coarse elongated grains can be observed in the DEDed Ti-5553 without any precipitates or cracks in both SEM BSE image in Fig. 3(a) and the inverse pole figure (IPF) mapping in Fig. 3(b). The measured average grain size is approximately 210 µm in diameter, with an average aspect ratio of approximately 3.45, indicating the formation of coarse columnar β grains in Ti-5553 during DED process. The kernel average misorientation (KAM) mapping, averaged over a 3×3 pixel grid, showing the local misorientation distribution of the DEDed Ti-5553 from 0 to 5°, is presented in Fig. 3(c). In several β -grains, a 2–3° misorientation is observed in the interior and near the grain boundary, revealing residual stress in these β -grains. In comparison, in the β-solutionized and quenched casted Ti-5553, bcc structured $\boldsymbol{\beta}$ grains with an almost equiaxed morphology are observed in the IPF mapping in supplementary Fig. S1(a). In the corresponding KAM mapping (Fig. S1(b)), minimal misorientation in local regions in the interior of the β grains is present in the $\beta\text{-solutionized}$ Ti-5553. The above comparison indicates significantly higher residual stress in the coarse columnar β grains in the DEDed Ti-5553 compared to the equiaxed β grains in the β -solutionized cast Ti-5553 alloy.

In order to investigate the texture in the DEDed Ti-5553 sample, a large area EBSD scan (\sim 5 mm \times 5 mm) with the beam parallel to the build direction was conducted. The IPF mapping in Fig. 4(a) shows only

 β grains in the DEDed Ti-5553, consistent with the result in the IPF mapping in Fig. 3(b). The top-view grain texture mapping of the β grains in Fig. 4(b-d) reveal that there is no significant texture in any direction in the DEDed Ti-5553. Based on the SEM BSE imaging and EBSD analysis, no α precipitates were found in the DEDed Ti-5553. Thus, in the DEDed Ti-5553, coarse columnar β grains with high residual stress and no texture are formed without any α precipitates. It is worth noting that several studies have reported the observation of α precipitates at the bottom layers of as-built metastable Ti alloys as a result of the cyclic reheating process [17]. The divergence observed between our findings and those reported in literature could be attributed to the diminished effect of intrinsic heat treatment, which in our case may result from the relatively small sample size utilized.

The nanoscale structure in the interior of the coarse columnar β grains in the DEDed Ti-5553 was investigated using TEM, as shown in Fig. 5. TEM SADPs and corresponding dark field images were obtained with the electron beam parallel to the $[110]_{\beta}$, $[\overline{1} \ \overline{3} \ 1]_{\beta}$, and $[001]_{\beta}$ directions. In the $[110]_{\beta}$ and $[\overline{1} \ \overline{3} \ 1]_{\beta}$ zone axis SADPs, in addition to hexagonal structured ω phase reflections located at 1/3 and 2/3 {112}₆, additional reflections near ½ of {112}₆ can be observed, demonstrated in the line intensity profile (insets in Fig. 5(a-b)) along the red dotted arrows. Such additional reflections may belong to either orthorhombic structured O' phase or orthorhombic structured α'' phase. The corresponding DF images collected by selecting the reflections in the blue color circles in Fig. 5(a-b) are shown in Fig. 5(d-e). Nanoscale particles with a diameter less than 5 nm can be observed almost homogeneously distributed in the interior of the β grain without the presence of any plate morphology martensite. Thus, the additional reflections observed near ½ of {112}₆ belong to the orthorhombic structured O' phase. Additionally, SADPs were collected on $[001]_6$ to further validate the presence of O' phase. On the [001]₆ zone axis SADP, weak O' reflections can be seen at $\frac{1}{2}$ of $\{310\}_{\beta}$, consistent with the inset line profile across the red arrow, shown in Fig. 5(c). By selecting the O' reflection in the blue circle, O' phase nanoprecipitates are further confirmed to form in the interior of

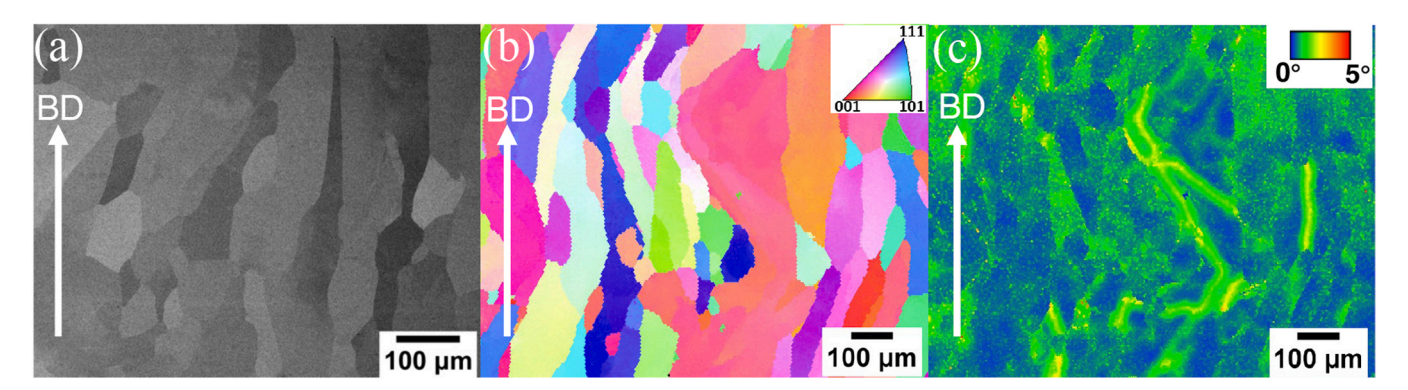


Fig. 3. EBSD analysis from DEDed Ti-5553: (a) SEM BSE image and (b) EBSD IPF mapping showing columnar β grains; (c) Kernel average misorientation (KAM) mapping showing the misorientation present in β grains.

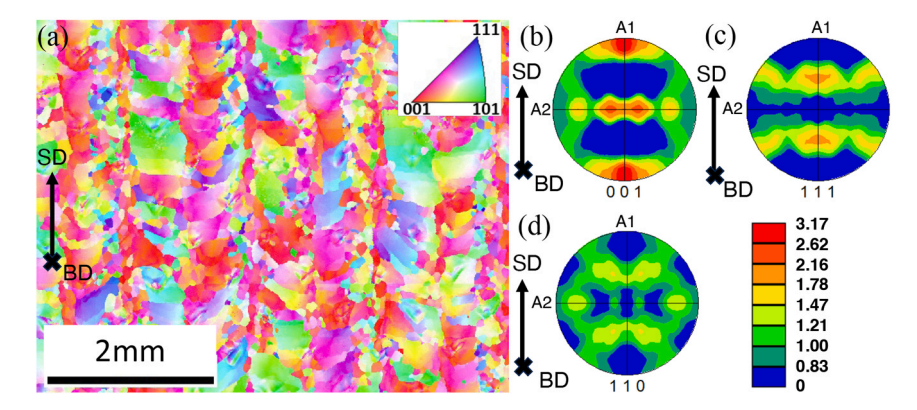


Fig. 4. Large area EBSD analysis from DEDed Ti-5553: (a) IPF mapping showing β grains in a 5 mm \times 5 mm area; (b-d) (001), (110) and (111) plane grain texture mappings showing no texture in β grains.

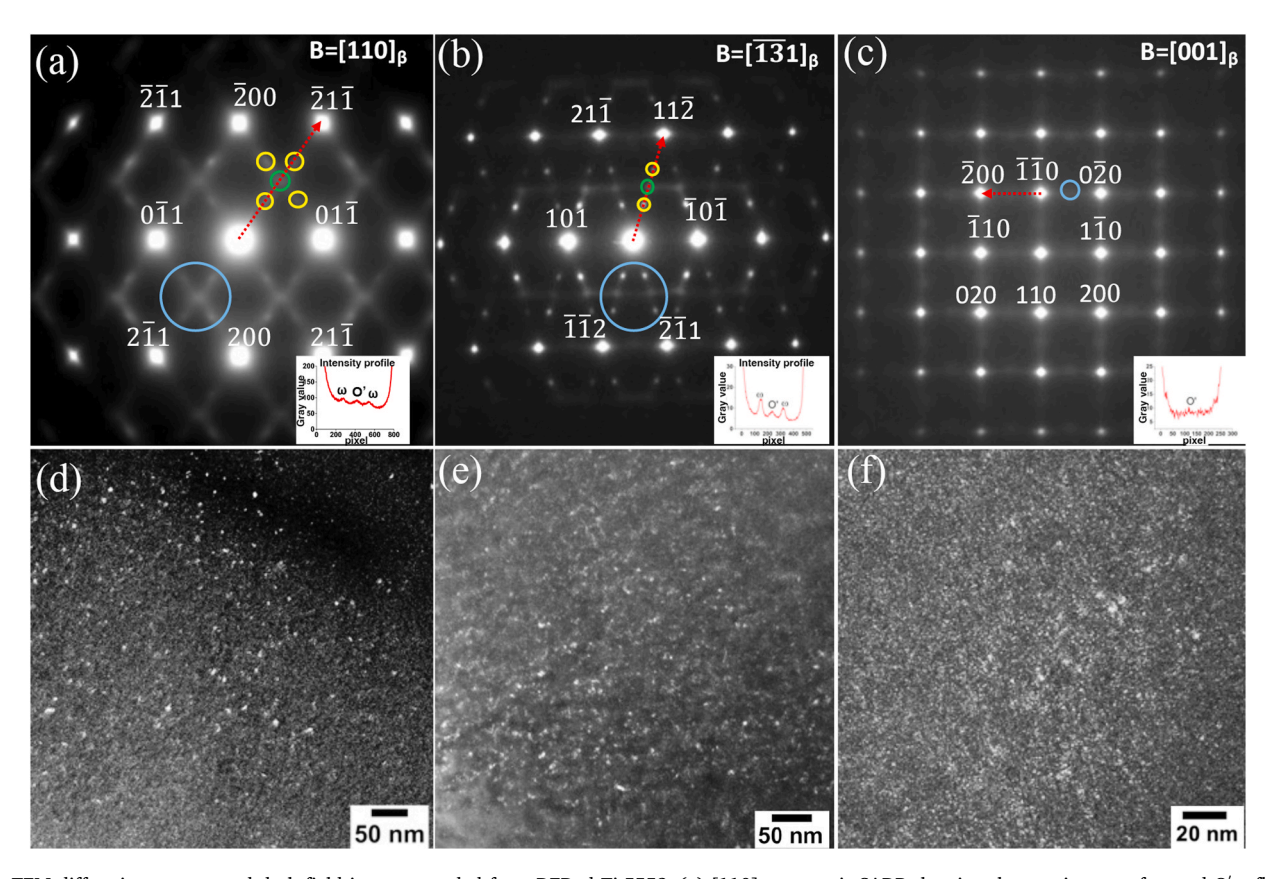


Fig. 5. TEM diffraction pattern and dark field image recorded from DEDed Ti-5553: (a) $[110]_{\beta}$ zone axis SADP showing the coexistence of ω , and O' reflections, marked using yellow color and blue color circles respectively, and line profile along the red color dotted line (inset) showing the maxima at 1/3, 1/2, and 2/3 of $\{112\}_{\beta}$; (b) $[\overline{1} \ \overline{3}\ 1]_{\beta}$ zone axis SADP with markers showing using ω reflections in yellow color and O' reflections in blue color circles respectively, and with inset line profile along the red color dotted line; (c) $[001]_{\beta}$ zone axis SADP showing the O' reflections at ½ of $\{310\}_{\beta}$ marked in blue and the line profile (noted by a red arrow); (d) corresponding dark field image collected by selecting reflections marked using the blue color circle in (a) showing the nanoscale ω and O' particles; (e) corresponding dark field image collected by selecting reflections marked using the blue color circle in (b) showing the nanoscale ω and O' particles; (f) corresponding dark field image collected by selecting marked using the blue color circle in (c) showing O' particles.

the β grain. Our experimental results, displayed in Fig. 5(a-f), have revealed for the first time that nanoscale ω phase with hexagonal structure and O' phase with orthorhombic structure are formed in the interior of coarse columnar β grains in DEDed Ti-5553. It is worthy to point out that the observed nanoscale $\omega+$ O' phases in the DEDed Ti-5553 are similar to the nanostructures observed in the β grains in the β -solutionized cast Ti-5553 alloy [47] and other metastable β -Ti alloys [48–50], in which experimental results have shown that these nanoscale structure may influence the subsequent α precipitation and refine the α

microstructure [25,26,29,50].

The oxygen concentration in the DEDed Ti-5553 has been evaluated using LECO ON736 chemical analyzer, determining it to be approximately 0.123 ± 0.005 wt%. Compared to the oxygen content measured in the Ti-5553 powders, there is an approximately 67 % increase in oxygen concentration, from 0.0737 wt% in the powders to 0.123 wt% in the DEDed Ti-5553 sample. This increase in oxygen concentration in the as-built sample can be attributed to potential oxygen pickup during the DED process. Similar oxygen pickup in titanium alloys such as Ti-6Al-

4 V and Ti-6Al-2Sn-4Zr-2Mo-Si during the DED process has been reported in literature [51,52].

The composition of the DEDed Ti-5553 was further analyzed utilizing 3D APT. To eliminate the surface contamination effects, a 25 \times 25 \times 25 nm³ cube was selected (Fig. 7(b)) within the core of the reconstructed needle for bulk composition and cluster analysis. The bulk composition of the sample was determined to be Ti-4.7Al-5.1 V-5.3Mo-2.9Cr (wt%) or Ti-8.2Al-4.7 V-2.6Mo-2.6Cr (at%) with an oxygen concentration of approximately 0.2 wt% (0.6 at%), as shown in Table 1. Although there is a difference in oxygen concentration measured from LECO chemical analyzer and 3D APT, which could be attributed to possible oxygen absorption during the APT needle preparation, the oxygen concentration measured using 3D APT further validates the increase in oxygen concentration in the DEDed Ti-5553 and confirms the oxygen pickup during the DED process. The APT data was then analyzed by visually inspecting the raw ion maps and employing proxigrams to detect any elemental segregation or the presence of clustered/ordered domains, shown in Fig. 6. Fig. 6(a) shows the 3D raw ion map of Ti, Al, V, Mo, and Cr ions throughout the sample, displaying 2.15 % of total Ti ions, 20 % of total Al ions, 35 % of total V ions, 61 % of total Cr ions, and 100 % of total Mo ions. The raw ion map does not reveal any obvious solute segregation. However, a proximity histogram (proxigram) extracted from the APT data was plotted across the 79.4 at% Ti iso-concentration surface, as shown in Fig. 6(b-c). The plot shows that there exist some nanoscale domains in DEDed Ti-5553, where the Ti concentration increases from \sim 76 at% to \sim 82 at%. At the same time, the solute atoms are found to be depleted in these nanoscale domains. The content of Al, V, Mo and Cr depletes from 8.4 at%, 4.9 at%, 2.7 at% and 3.3 at% in the β phase matrix to 7.5 at%, 4.5 at%, 1.8 at% and 2.5 at%, respectively within the nanoscale domains. The proxigram plot also reveals a slight segregation of the rejected Al and Mo atoms from the nanoscale domains, at their interface with the β matrix. Additionally, a substantial oxygen enrichment in the β phase region is revealed by the proxigram, with oxygen concentration increasing from 0.5 at% in the Ti-rich nanoscale domains to approximately \sim 2.5 at% in the β phase region.

Subsequently, frequency and radial distribution analyses were conducted on selected elements within a volume of $25 \times 25 \times 25 \text{ nm}^3$ exported from the original APT reconstruction, shown in Fig. 7. In frequency distribution analysis, the exported volume is divided into voxels, each containing N ions (N = 100 in this case). The mole fraction of each element in a voxel is depicted as a frequency distribution histogram. The clustering of elements can be identified by comparing the measured distribution of the element with the theoretical binomial distribution. Fig. 7(a) shows the frequency distribution plot of Ti atoms as a function of its mole fraction. Element clustering can be identified by comparing the observed distribution of the element with the expected binomial distribution. The plot compares the observed Ti atom distribution to the random binomial distribution in the sample and shows that both curves peaked at an approximate Ti mole fraction of 0.81. The noticeable deviation of the observed curve from the binomial curve indicates the presence of clustered/ordered domains. Radial distribution analysis, on the other hand, calculates the concentration of elements as a function of

Table 1 Composition of bulk, β phase, and cluster measured using APT in the DEDed Ti-5553.

Element	Composition (at%)				
	Bulk	β phase	Cluster		
Ti	80.0	78.9	88.9		
Al	8.0	9.0	4.6		
V	4.7	5.0	3.2		
Mo	2.4	2.9	1.3		
Cr	2.7	2.9	1.4		
0	0.6	0.7	0.2		
N	0.1	0.1	0.0		
H	0.5	0.6	0.3		

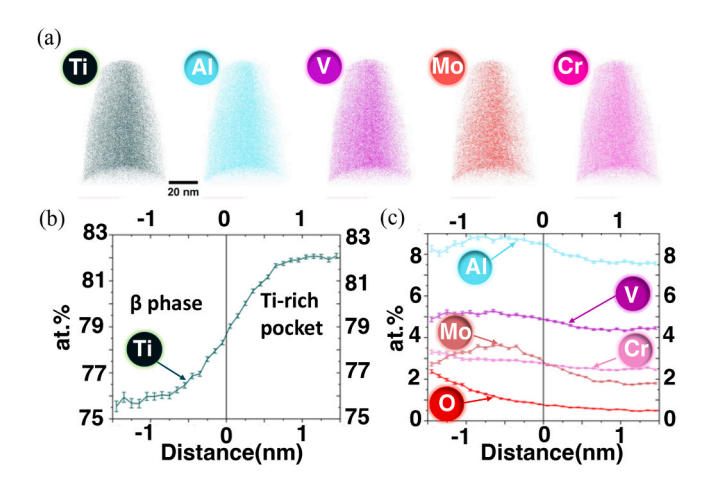


Fig. 6. APT reconstruction showing the distribution of Ti, Al, V, Mo and Cr atoms in DEDed Ti-5553: (a) Raw ion map showing the distribution of Ti, Al, V, Mo, and Cr ions; (b) Proxigram across the 79.4 at% Ti iso-concentration surface showing the presence of Ti-rich and solute-lean region.

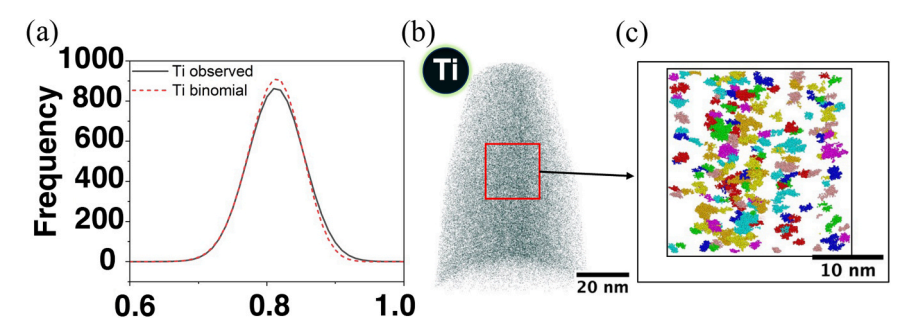
radial distance from a specified center element. When the frequency or radial distribution suggests the possibility of clustering/ordering, cluster analysis is performed to reveal qualitative and quantitative details of the clusters using the maximum separation method. This method involves selecting a maximum separation distance between clustered/ordered element(s) and a minimum number of ions in the cluster based on the nearest neighbor distribution, cluster size, and cluster count distributions. A $25 \times 25 \times 25$ nm³ cubic volume (marked as a red square in Fig. 7(b)) was exported from the core region of the original 3D reconstruction and analyzed for any possible clusters present and further analyzed using cluster analysis. Fig. 7(c) shows the Ti-rich clusters formed uniformly throughout the sample with an average diameter of approximately 1.3 nm. Moreover, the average composition of the cluster and matrix is given in Table 1. The clusters were formed by the concurrent depletion of solute atoms and enrichment of Ti atoms, which is in agreement with the proxigram results in Fig. 6(b-c). The concentration of Ti increased to 88.9 at% in the Ti-rich pockets compared to the matrix composition of 78.9 at%. Additionally, the concentration of Al, V, Mo and Cr atoms were depleted in the Ti-rich pockets to 4.6 at%, 3.2 at%, 1.3 at%, and 1.4 at% respectively. In the authors' previous studies of isothermal ω phase particles in cast Ti-5553 after aging using APT, it has been found that all solutes including the α phase stabilizer Al, and β phase stabilizers Mo, V, and Cr, are all rejected from the nanoscale isothermal ω precipitates into the adjacent β phase [29,53]. Thus, the observed nanoscale Ti-rich and solute-lean clusters are likely to be early stages of formation of isothermal ω precipitates, formed in Ti-5553 during DED process. Coupling the results from the SEM, TEM, and 3D APT investigations, clearly establishes the presence of nanoscale isothermal ω precipitates and O' precipitates in the β phase in DEDed Ti-5553.

3.3. Microstructure in post-heat treated Ti-5553

To assess the influence of nanoscale isothermal ω phase and O' phase particles formed during the DED process on α precipitation during postheat treatments of DEDed Ti-5553, two groups of post-heat treatment were performed, and the microstructure was characterized using SEM, TEM, and STEM.

3.3.1. Microstructure in DEDed Ti-5553 after isothermal aging at different temperatures

The first group of post-heat treatment focused on the influence of different aging temperatures on the final α microstructure in DEDed Ti-5553. The microstructures of DEDed Ti-5553 after being isothermally



aged at 600°C, 700°C, and 800°C were characterized using SEM BSE imaging and quantitatively analyzed using MIPARTM image analysis software (Fig. 8(a-i)). In the DEDed Ti-5553 isothermally aged at 600°C, plate morphology α precipitates are observed almost uniformly distributed in the interior of the β grains in Fig. 8(a-b). These α plates form a triangular shape cluster for three variants or chevron shape cluster for two variants with the length along the longest direction, $\sim 1~\mu m$. Fig. 8 (c) is the image processed using MIPARTM in an attempt to quantify the fraction, sizescale, and number density of α precipitates. It is found that the number density of α plates is approximately $10.7\pm1.1~ppts/\mu m^2$, consistent with the so-called refined α microstructure in cast Ti-5553 aged at the same temperature [24]. In the DEDed Ti-5553 isothermally aged at 700°C, plate morphology α precipitates of similar sizescale are observed to form with reduced area fraction and $\sim 1~\mu m$ in length, in

Fig. 8(d-e). Similar triangular or chevron shape clusters of α precipitates were observed. The number density of α plates is approximately 6.2 ± 0.6 ppts/ μm^2 in Fig. 8(f). Notably, compared to cast Ti-5553 aged at 700°C [54], DEDed Ti-5553 displays a much finer α microstructure with a higher number density and a smaller sizescale. Further analysis using EBSD techniques shown in supplementary Fig. S2 reveals that these α precipitates follow the Burgers orientation relationship with parent β phase but don't exhibit any specific texture. In the DEDed Ti-5553 isothermally aged at 800°C, the morphology of α precipitates shows dramatic change. The lengths of the α precipitates vary from several micrometers to tens of micrometers, and the interface between α precipitate and β matrix is not smooth but exhibits irregular morphology. Two or three α variants are still observed to intersect with each other to form a chevron shape or a triangularly shaped cluster, in Fig. 8(g-h). The

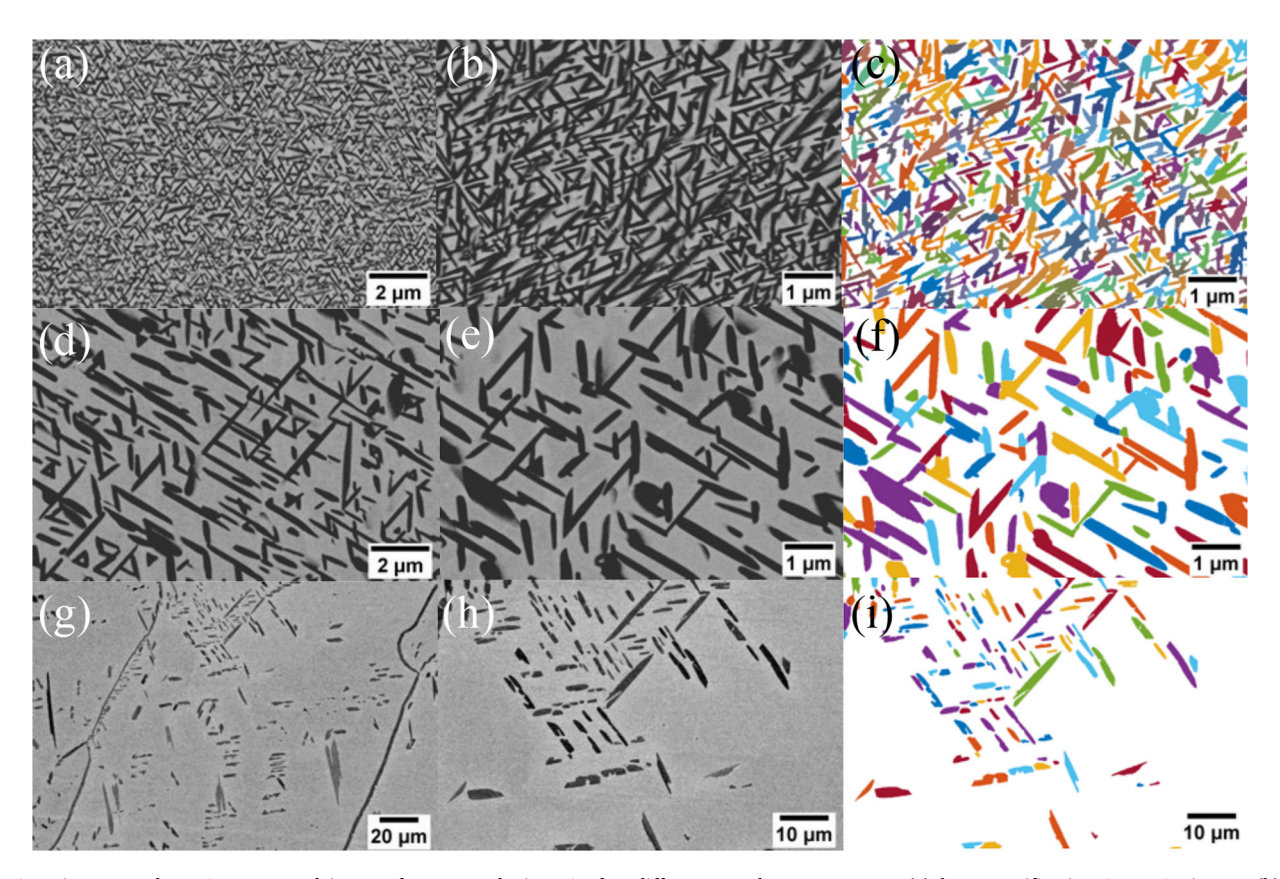


Fig. 8. SEM images and MIPAR processed images from DEDed Ti-5553 after different post-heat treatments: (a) low-magnification SEM BSE image, (b) high-magnification SEM BSE image, and (c) MIPAR processed image of (b) from DEDed Ti-5553 showing refined α microstructure after up-quenching to 600°C, isothermally held for 2 hours, and rapidly water quenched to room temperature; (d) low-magnification SEM BSE image, (e) high-magnification SEM BSE image, and (f) MIPAR processed image of (e) from DEDed Ti-5553 showing fine-scaled α microstructure after up-quenching to 700°C, isothermally held for 2 hours, and rapidly water quenched to room temperature; (g) low-magnification SEM BSE image, (h) high-magnification SEM BSE image, and (i) MIPAR processed image of (h) from DEDed Ti-5553 showing coarse α microstructure after up-quenching to 800°C, isothermally held for 2 hours, and rapidly water quenched to room temperature.

number density of α precipitates is approximately 0.02 ± 0.003 ppts/ μm^2 , in Fig. 8(i). The morphology, interface structure, and the number density of α precipitates in the DEDed Ti-5553 aged at 800° C are consistent with the so-called coarse α microstructure in cast Ti-5553 [55]. Thus, our experimental characterization demonstrates that adjusting aging temperature can effectively alter the α microstructure in the DEDed Ti-5553, forming refined α microstructure at 600° C and coarse α microstructure at 800° C.

In order to study the fine-scale α microstructure formed during isothermally aging at 700°C in the DEDed Ti-5553, 3D FIB-SEM tomography was applied to reveal the true 3D morphology of α precipitates. Fig. 9(a-d) show the reconstructed 3D microstructure in the DEDed Ti-5553 and cast Ti-5553 aged at 700°C for 2 hours with dimensions of 9.6 \times 7.5 \times 11 μm^3 , where individual α plates are marked using different colors in Figs. 9(a) and 9(c). In the DEDed Ti-5553, the α precipitates are almost uniformly distributed in Fig. 9(a). Two α variants form chevron shape cluster and three α variants form a triangular shape cluster, shown in Fig. 9(b). The average equivalent diameter and volume of those finer-scale α plates are 1.07 µm and 0.86 µm³, while the volume number density is 0.37 feature/µm³. On the other hand, in the cast Ti-5553, non-uniform α laths longer than 5 μ m in length shown in Fig. 9 (c) interconnect and branch to each other growing in specific directions presented in Fig. 9(d). Quantifications show that the average equivalent diameter and volume in cast Ti-5553 are 1.84 μm and 5.43 μm³, with a reduced volume number density of 0.07 feature/µm³. To compare, the average volume of α plates from DEDed sample is less than 20 % of the those in cast Ti-5553 while the number density increases by five times, indicating a significant refinement of α microstructure in the DEDed Ti-5553. Thus, the characterization from 2D SEM BSE imaging and 3D FIB-SEM tomography show that the α microstructure formed at 700°C in the DEDed Ti-5553 is significantly different from that in cast Ti-5553, with a much higher number density and dramatically smaller sizescale.

3.3.2. The microstructure in the DEDed Ti-5553 after isothermal aging at different heating rates

The second group of post-heat treatment focused on the influence of different heating rates on the final α microstructure in the DEDed Ti-5553. The microstructure in DEDed Ti-5553 while heating to 600°C at

the rates of 5 °C/min and 0.5 °C/min was investigated using SEM BSE imaging and shown in Fig. 10(a-f). In the DEDed Ti-5553 heated at 5 °C/ min, much finer α precipitates are observed and shown in Fig. 10(a-b). Compared with the α microstructure in the up-quenched sample (Fig. 8 (a)), the lengths of the α precipitates are approximately 300–500 nm along the long axis direction. To further validate the influence of the heating rate on the α microstructure formed, another DEDed Ti-5553 sample was heated to the 600°C at the rate of 0.5 °C/min. Fig. 10(d-e) reveal that the sizescale of α precipitates is even finer, with the length of the α plates ~200 nm along the long axis direction. It is also worthy to point out, with the decrease of α plate's size, the micro-texture of the α plates is even more difficult to observe. Compared to the refined α microstructure formed in the DEDed Ti-5553 in Fig. 8(a-b), the α microstructure formed in the DEDed Ti-5553 during slow heating shows much higher number density, $30.2\pm0.9~\text{ppts/}\mu\text{m}^2$ and $47.8\pm0.8~\text{ppts/}$ μm², respectively when the heating rate of 5 °C/min and 0.5 °C/min were adopted, similar to the so-called super-refined $\boldsymbol{\alpha}$ microstructure in the cast Ti-5553 [29].

Due to α precipitates being extremely small in sizescale, the structure and the composition of α precipitates in super-refined α microstructure in the DEDed Ti-5553 while heating to 600°C at the rate of 0.5 °C/min were further analyzed in detail using TEM and STEM, shown in Figs. 11–12. In the $[\overline{1}11]_{6}$ zone axis SADP (Fig. 11(a)), clear α reflections are observed at $\frac{1}{2}$ {110} $_{\beta}$ reflections marked in yellow circles. The corresponding DF image selecting one α diffraction in Fig. 11(b) shows super-refined α plates with 300–500 nm in length uniformly distributed in the β matrix. STEM EDS mappings in Fig. 12(a-f) indicate that the solute diffusion occurs between α precipitates and the parent β matrix. Ti and Al are observed enriched in the super-refined α plates and on the other hand, Mo, V and Cr are observed to be rejected in the parent β matrix. Thus, our experimental characterization results combining the SEM, TEM and S/TEM in Figs. 10-12 indicate that heating rates in the post-heat treatment of DEDed Ti-5553 can significantly alter the α precipitate microstructure. Specifically, a lower heating rate adopted results in a finer α microstructure and a higher number density of α precipitates in the DEDed Ti-5553.

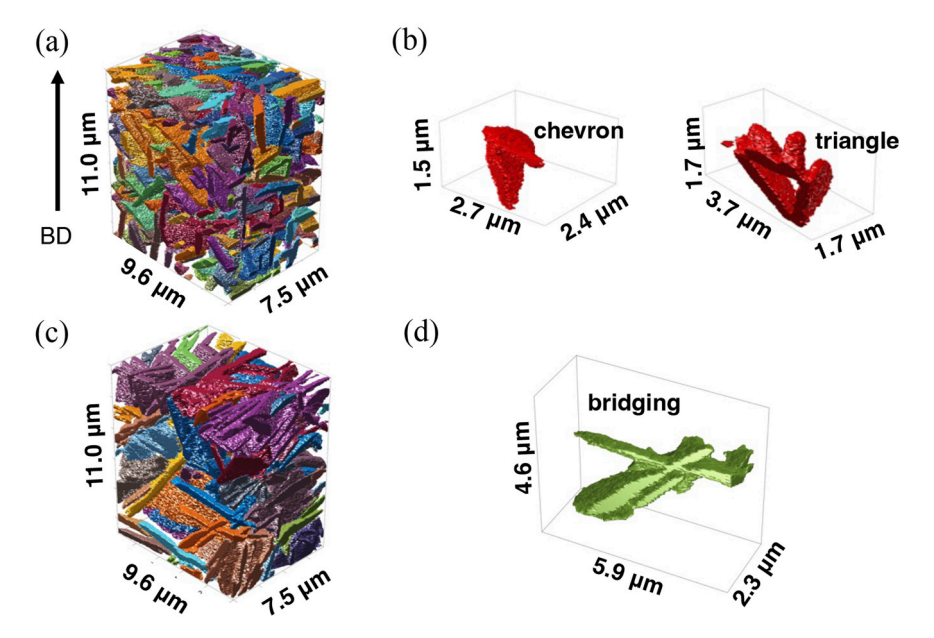


Fig. 9. 3D FIB-SEM tomography reconstruction showing different α microstructures from DEDed Ti-5553 and cast Ti-5553 alloys: (a) 3D reconstruction showing fine-scaled α microstructure in the volume of 9.6 × 7.5 × 11 μm³ from DEDed Ti-5553; (b) 3D reconstruction showing the chevron shape cluster of two α variants and triangle shape cluster of three α variants from DEDed Ti-5553; (c) 3D reconstruction showing coarse α microstructure in the volume of 9.6 × 7.5 × 11 μm³ from cast Ti-5553; (d) 3D reconstruction showing the intersection of two α variants from cast Ti-5553.

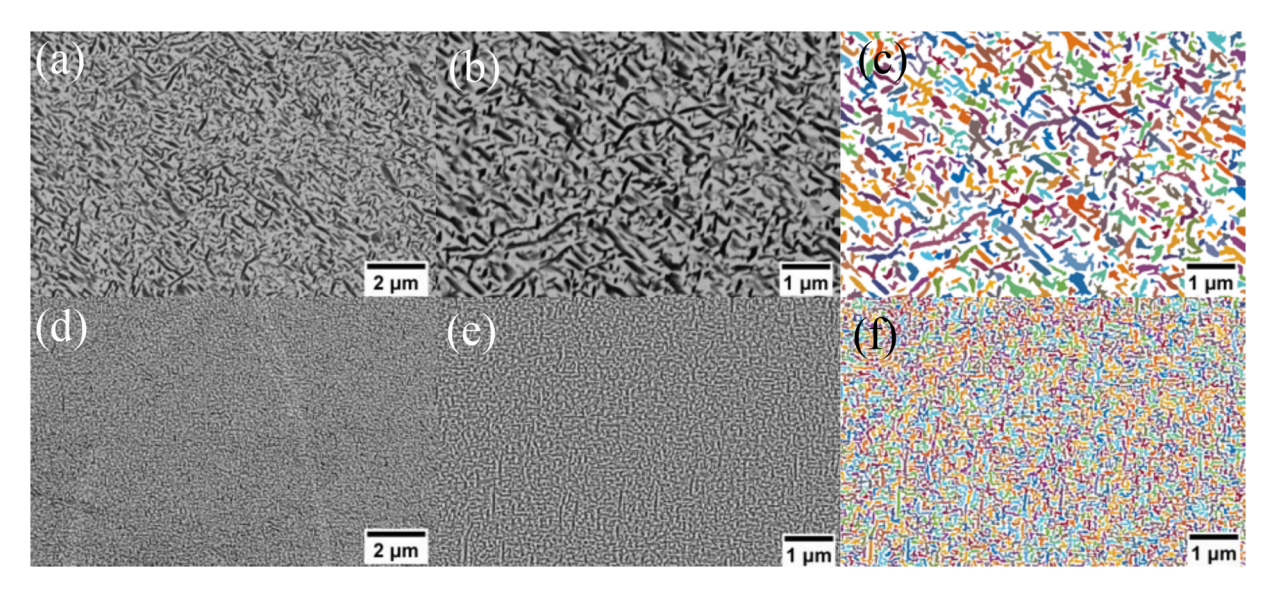


Fig. 10. SEM images and MIPAR processed images from DEDed Ti-5553 after different post-heat treatments: (a) low-magnification SEM BSE image, (b) high-magnification SEM BSE image, and (c) MIPAR processed image of (b) from DEDed Ti-5553 showing refined α microstructure after slow heated at 5 °C/min to 600°C, isothermally held for 2 hours, and rapidly water quenched to room temperature; (d) low-magnification SEM BSE image, (e) high-magnification SEM BSE image, and (f) MIPAR processed image of (e) from DEDed Ti-5553 showing fine-scaled α microstructure after slow heated at 0.5 °C/min to 600°C, isothermally held for 2 hours, and water quenched to room temperature.

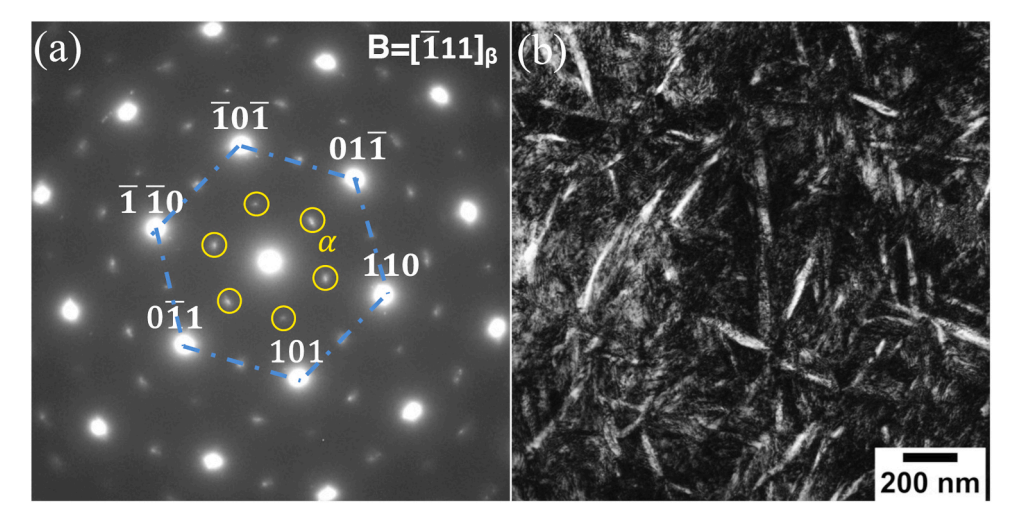


Fig. 11. TEM SADP and corresponding dark-field imaging showing super-refined α microstructure in the post-heat treated Ti-5553: (a) $[\bar{1}11]_{\beta}$ zone axis SADP with α reflections marked in yellow circles; (b) corresponding dark-field image by selecting one α reflection in (a).

3.4. Mechanical properties of DEDed Ti-5553 with and without post-heat treatment

The mechanical properties of post-heat treated and DEDed Ti-5553 were evaluated using Vickers hardness tests and room-temperature tensile tests. The initial hardness of the DEDed Ti-5553 is approximately 296 ± 5.64 HV. After the post-heat treatment, the hardness increased to 406 ± 4.6 HV, 368 ± 5.6 HV, and 332 ± 6.6 HV for isothermal aging at 600°C , 700°C , and 800°C , respectively. Additionally, the hardness increased to as high as 443 ± 9.7 HV and 458 ± 1.6 HV for samples subjected to a heating rate of 5 °C/min and 0.5 °C/min, respectively. The hardness test results are shown in Fig. 13 and summarized in Table 2.

Tensile tests were performed on DEDed Ti-5553 with and without post-heat treatments. The measured stress-strain curves are presented in Fig. 14(a-b) and the measured yield strength, ultimate strength, and total elongation at fracture are summarized in Table 2. The DEDed Ti-5553 exhibits a total elongation at fracture of $19.1\pm1.0~\%$ with a yield

strength of 809.0 \pm 75.0 MPa and ultimate strength of 858.3 \pm 49.9 MPa. Additionally, the Young's modulus of DEDed Ti-5553 measured using nanoindentation is 79.1 \pm 2.0 GPa. The above measured values in our tensile test using miniature specimens are comparable to the values reported from the laser-based additively manufactured Ti-5553 [18,56,57]. Isothermal aging at 600°C, 700°C, and 800°C results in the increased yield strength and ultimate strength of 1425.5 \pm 54.0 MPa and 1477.5 \pm 49.9 MPa. 1079.4 \pm 50.5 MPa and 1120.6 \pm 63.9 MPa, and 857.2 \pm 55.4 MPa and 913.6 \pm 44.1 MPa, respectively, accompanied by a decrease in total elongation to approximately 3.7 \pm 0.1 %, 6.6 \pm 0.5 %, and 10.4 \pm 1.8 %, in Fig. 14(a). For the sample heated at the rate of 5 °C/min, the yield strength and ultimate strength further increase to 1460.6±60.0 MPa and 1534.6 ± 46.1 MPa with reduced total elongation to only 3.6 \pm 5.6 %, in Fig. 14 (b). Remarkably, the sample heated at the rate of 0.5 °C/min exhibited extreme brittleness, failing before reaching the yield limit. These tensile test results clearly emphasize that post-heat treatment can significantly modify the mechanical performance of DEDed Ti-5553, with both aging

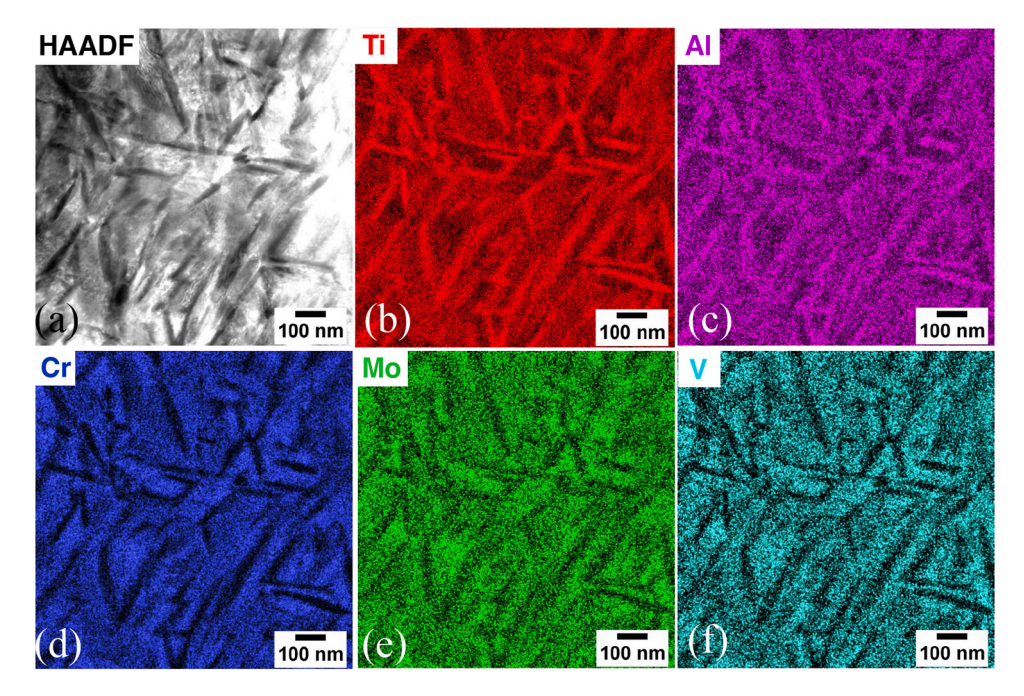


Fig. 12. HAADF-STEM imaging and XEDS mapping showing super-refined α microstructure in the post-heat treated Ti-5553: (a) HAADF-STEM image; XEDS mapping showing the distribution of elements (b) Ti; (c) Al; (d) Cr; (e) Mo; and (f) V.

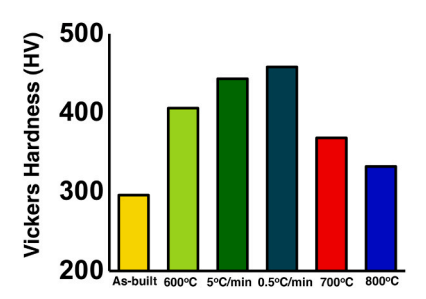


Fig. 13. Vickers hardness of Ti-5553 after different post-heat treatments.

temperature and heating rates altering the yield strength, ultimate strength, and total elongation.

The morphology of the fracture surfaces of the DEDed Ti-5553 after tensile tests were characterized using SEM SE imaging, presented in Fig. 15(a-e). DEDed Ti-5553, along with samples aged at 800°C and 700°C, display a mixture of dimples (marked in orange color) and shear lips (marked in yellow color), indictive of ductile fracture in Fig. 15 (a-c, f-h). Conversely, river-patterned facets (marked in green color) are characterized in the up-quenched or slowly heated to 600°C Ti-5553 in Fig. 15(d-e, i-j). The size of dimples decreases from 5 to 30 μm in the DEDed Ti-5553, to 3–15 μm in the 800°C aged Ti-5553, and 1–2 μm in the 700°C aged Ti-5553, consistent with the size of α precipitates in these samples. Finer-scaled dimples are observed from the sample up-quenched to 600°C, while an insufficient number of dimples are

observed in the sample slowly heated to 600° C. These observations suggest that ductile fracture occurs in the DED Ti-5553 and high-temperature aged Ti-5553 (700° C and 800° C); while in contrast, cleavage mode dominates the fracture in the samples aged at 600° C regardless of heating rate, consistent with the lack of ductility observed in the tensile testing results. Thus, fracture analysis evidently shows that different fracture modes occur in the post-heat treated Ti-5553, accounting for different combinations of strength and ductility in these samples.

4. Discussion

In addition to experimental results of microstructural features and mechanical properties, it is of specific importance to discuss the fundamental mechanisms responsible for the formation of various microstructures during DED and post-heat treatment of Ti-5553, aiming at gaining an in-depth understanding of the process-microstructure relationship and providing insights towards elucidating the effect of microstructural features on the tuned strength and ductility of 3D additively manufactured metastable β -Ti alloy.

4.1. Formation of isothermal ω phase and O' phase in the DEDed Ti-5553

Our experimental characterization combining SEM and TEM analysis has revealed for the first time the presence of nanoscale isothermal ω phase and O' phase in the interior of β grains with the absence of any α precipitates in the DEDed Ti-5553. Both isothermal ω phase and O' phase have been observed in a variety of cast metastable $\beta\textsc{-Ti}$ alloys during

Table 2Microstructure and mechanical properties of DEDed Ti-5553 with and without post-heat treatments.

Sample	Density of α (ppts/mm ²)	Hardness (HV)	Yield strength (MPa)	Ultimate strength (MPa)	Ductility (%)
DEDed Ti5553	N/A	296±5.6	809.0±75.0	858.3±75.0	19.1±1.0
600°C isothermal aging	$10.7{\pm}1.1$	406±4.6	1425.5 ± 54.0	1477.5 ± 49.9	$3.7 {\pm} 0.1$
700°C isothermal aging	$6.2 {\pm} 0.6$	$368 {\pm} 5.6$	1079.4 ± 50.5	1120.6 ± 63.9	6.6 ± 0.5
800°C isothermal aging	$0.02{\pm}0.003$	$332{\pm}6.6$	857.2±55.4	913.6 ± 44.1	$10.4 {\pm} 1.8$
0.5 °C/min heating rate	47.8±0.8	458±1.6	N/A	N/A	N/A
5 °C/min heating rate	$30.2{\pm}0.9$	443±9.7	1460.6 ± 60.0	1534.6 ± 46.1	3.6 ± 5.6

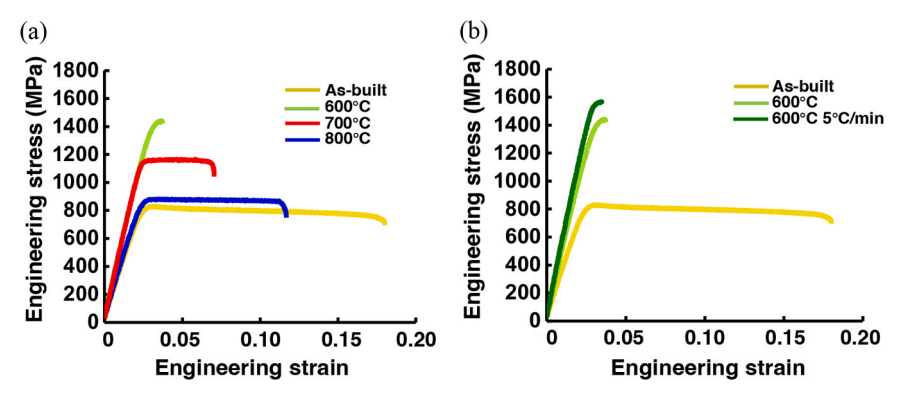


Fig. 14. Tensile stress-strain profiles of DEDed Ti-5553 after different post-heat treatment: (a) stress-strain profiles of DEDed Ti-5553 after being isothermally aged at 600°C, 700°C and 800°C; (b) stress-strain profiles of DEDed Ti-5553 after being heated up to 600°C at different heating rates.

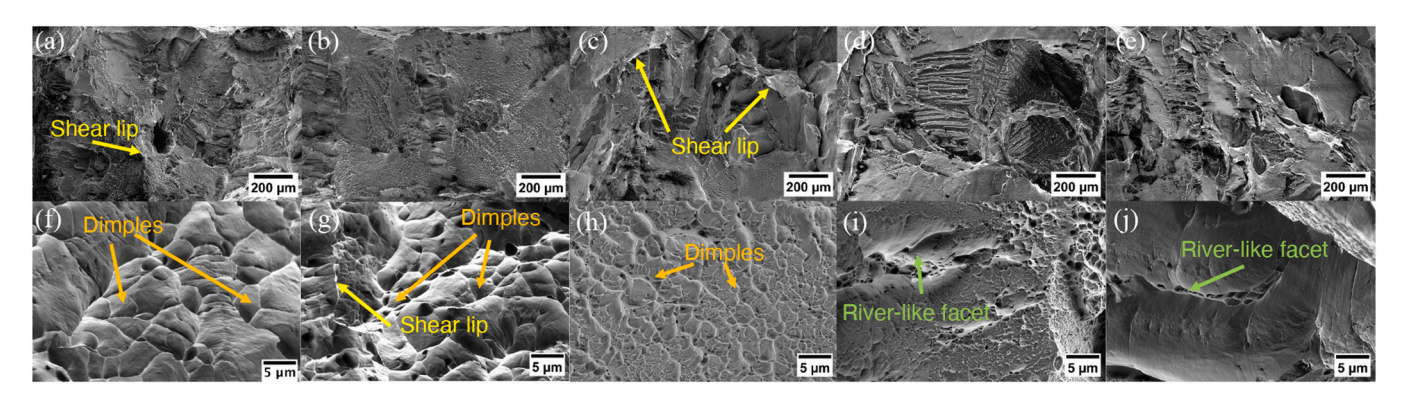


Fig. 15. SEM SE imaging at low and high magnifications showing the fractured surface tomography of DEDed Ti-5553 after different post-heat treatment: (a) and (f) DEDed Ti-5553; (b) and (g) DEDed Ti-5553 after isothermally aged at 800°C; (c) and (h) DEDed Ti-5553 after isothermally aged at 700°C showing dimples and shear lips marked in orange and yellow color respectively; (d) and (i) DEDed Ti-5553 after isothermally aged at 600°C; (e) and (j) DEDed Ti-5553 after being slowly heated (at a rate of 0.5 °C/min) to 600°C showing river-like facets marked in green color.

low-temperature aging and rapid cooling from above the T_β temperature to room temperature through different transformation mechanisms, shown in Fig. 16(a-b) [49,58,59]. The duplex diffusional and displacive β to isothermal ω phase transformation involves the shuffling of atoms on every two of three adjacent $\{111\}_\beta$ planes towards each other, marked by red color arrows in Fig. 16(a), leaving the third plane

unchanged, and solute diffusion between isothermal ω phase and the parent β phase matrix. Depending on the alloys' solute content, the shuffled atoms may or may not reach the intermediate plane to transform the parent bcc structure to hexagonal structure [60,61]. On the other hand, if the solute content surpasses a critical composition in metastable β -Ti alloys, the diffusionless transformation from β to O'

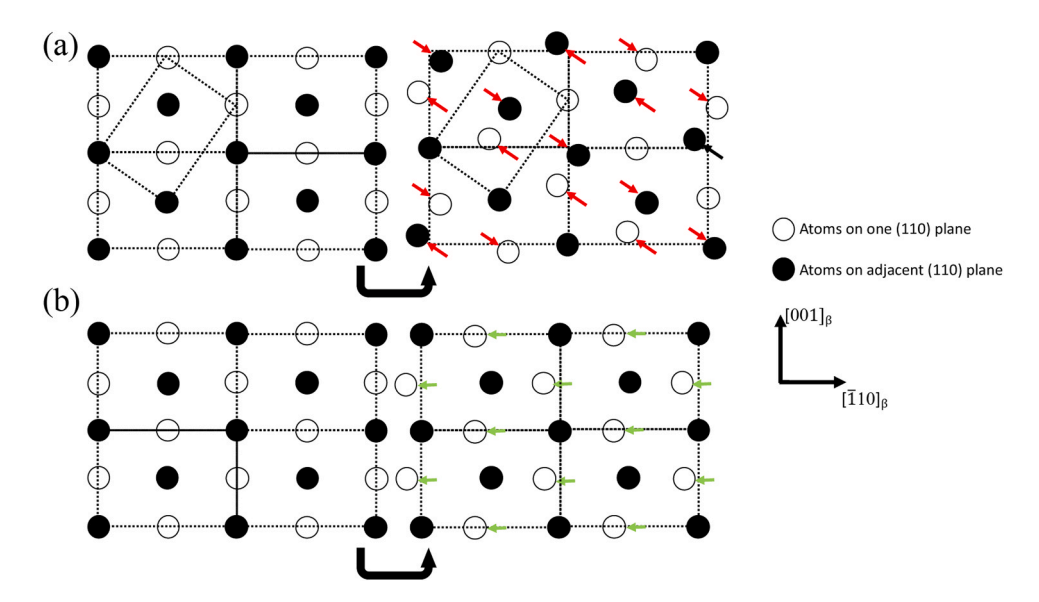


Fig. 16. Schematic drawings showing the atom shuffle in different shuffle transformations: (a) atoms on every two of three adjacent $\{111\}_{\beta}$ planes shuffling towards each other in β to ω transformation; (b) atoms on every other $\{1\overline{10}\}_{\beta}$ planes shuffle along $<110>_{\beta}$ direction in β to 0' transformation.

phase can occur via the shuffling of atoms on every other $\{110\}_{\beta}$ planes along the $<1-10>_{\beta}$ direction, marked by green color arrows in Fig. 16 (b), changing the parent bcc structure to the orthorhombic structure [48, 62]. Notably, compared to the martensitic β to orthorhombic α'' phase transformation, the formation of orthorhombic O' phase lacks a shear component, resulting in little or almost no strain involvement [63,64].

During the DED process of Ti-5553, the rapid cooling rate of typically 10^3 - 10^5 °C/s effectively suppresses diffusional phase transformation, e. g., α phase precipitation from β phase [65]. However, such a rapid cooling process allows the formation of diffusionless ω and O' phases. It is crucial to highlight that the periodic reheating on previously deposited layers during the DED process may influence the $\boldsymbol{\omega}$ phase formed in DEDed Ti-5553 by transforming the so-called athermal ω phase to isothermal ω phase. In cast Ti-5553, during low-temperature aging, e.g., isothermally aged at 350°C or continuously heated up to 350°C, solute diffusion could occur between the ω phase and parent β phase and transform the athermal ω phase formed during rapid quenching to the isothermal ω phase formed during aging. In DEDed Ti-5553, the reheating cycles may facilitate similar diffusion occurring between the athermal ω phase formed during rapid cooling and thus form the isothermal ω phase. The isothermal ω phase forms from the athermal ω through the rejection of all the solute atoms into the adjacent beta matrix, which has been validated by the observed Ti-rich and solute lean pockets in the 3D APT reconstruction shown in Figs. 6-7.

Additionally, another novel metastable phase, O'' phase with ordered orthorhombic structure [66], has not yet been observed in the DEDed Ti-5553. The absence of ordering may be attributed to the limited aging time and constrained solute diffusion during the DED process. In contrast to the DEDed α/β Ti alloys, e.g. Ti-64 [67], there is no α' or α'' martensite formed in the DEDed metastable β Ti-5553. Thus, in the DEDed Ti-5553, nanoscale isothermal ω phase and O' phase are formed in the β phase matrix due to the high cooling rate and periodic heating involved, and our TEM results at three different zone axes validate the presence of both nanoscale phases. These nanostructures have the potential to significantly influence the microstructure evolution during subsequent post-heat treatment of the DEDed Ti-5553.

4.2. Formation of different α microstructures during post-heat treatments

4.2.1. Refined α microstructure

In DEDed Ti-5553, upon rapidly up-quenching and subsequent isothermally holding at 600°C for 2 hours, α microstructure emerges with a number density of $10.7\pm1.1~ppts/\mu m^2$. The characteristics of this α microstructure in the DEDed Ti-5553 including number density, sizescale, and morphology are comparable to the so-called refined α microstructure formed in cast metastable β -Ti alloys [24,30]. This similarity suggests that the refined α microstructure in the DEDed Ti-5553 may be formed through a pseudospinodal decomposition mechanism. In metastable β -Ti alloys, when the parent β phase has the average composition close to the intersection point of Gibbs free energy vs

composition curves of the parent β and product α phase at a given temperature, a small amplitude compositional fluctuation in the parent β phase will drive its composition into the opposite side of the intersection point, resulting in a driving force for the parent β phase to congruently transform into the product α phase. In such a situation, the system can reduce its Gibbs free energy via a rapid congruent transformation from parent β to the product α phase occurring within the small pockets created by the compositional fluctuations within the parent β phase. Subsequent compositional partitioning can occur between the parent β and the product α phase via long-range diffusion [24]. In order to verify the pseudospinodal decomposition mechanism, the Gibbs free energy curves for the α and β phases were plotted using Pandat software and are shown in Fig. 17. Using the Mo equivalency method, the calculated Mo equivalency for Ti-5553 is approximately \sim 9 wt% [24]. As shown in Fig. 17 (a-b), the intersection point is approximately 8.5 wt% at 600°C and 6.0 wt% at 700°C. Therefore at 600° C, the average composition of β phase in DEDed Ti-5553 is within the composition range where pseudospinodal decomposition can occur. The large amount of thermal compositional fluctuation in local areas in the interior of the β grains leads to a high number of nucleation sites for intragranular α precipitation. As a result, refined α microstructure with a large number density and small sizescale is formed inside the β grains. Importantly, the formation of the refined α microstructure during the post-heat treatment is unlikely to be related to the nanostructures, e.g., ω and O' particles in the DEDed Ti-5553. This is because during the rapid up-quenching to 600°C in DEDed Ti-5553, ω and O' phases will dissolve into parent β phase below 600°C. Thus, during the post-heat treatment of the DEDed Ti-5553, refined α microstructure is formed from the parent β phase directly likely via the pseudospinodal decomposition mechanism while up-quenching to 600°C and isothermally holding for 2 hours.

4.2.2. Fine scale α microstructure

In the DEDed Ti-5553, under the condition of rapidly up-quenching and isothermally holding at 700° C for 2 hours, a distinct fine-scale α microstructure with the number density of 6.2 ± 0.6 ppts/ μ m² is formed. Compared to the α microstructure formed during isothermal heat treatment at 700°C in cast Ti-5553, there is a clear difference in the morphology and sizescale of α microstructure formed in the DEDed Ti-5553. Comparing the 3D reconstructions from the FIB serial-sections shown in Fig. 9 for both the cast and DEDed Ti-5553 reveals that there are substantially more α nucleation sites in case of the latter. Considering the complexity of the thermo-kinetics involved in the DED process, it can be hypothesized that the fine-scale α microstructure may form due to the combination of multiple factors. These include both the indirect influence of nanoscale isothermal ω phase particles formed during DED process and the excess oxygen introduced during DED process. Firstly, during the rapid up-quenching to 700°C, the nanoscale isothermal ω precipitates may transform back to parent β phase as 700°C is substantially higher than the ω solvus temperature (~375°C) in Ti-

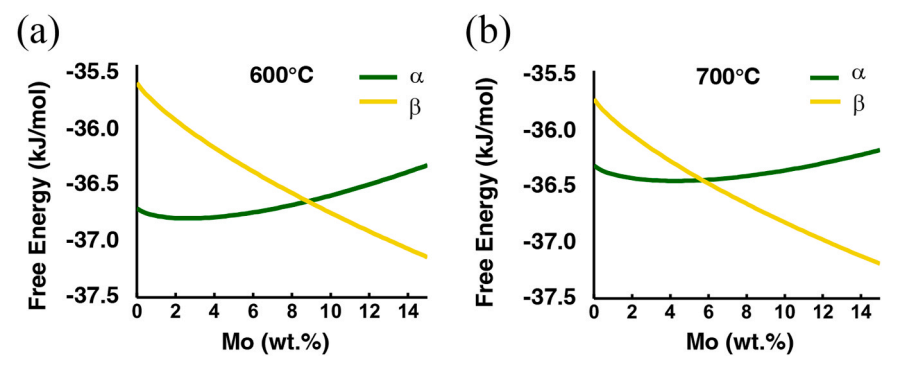


Fig. 17. Gibbs free energy curves for α and β phases in modeled Ti-Mo binary alloy at (a) 600°C and (b) 700°C.

5553. Given the relative short time available for this transformation, while the structural displacive (diffusionless) transition from the hexagonal structure to the body-centered cubic structure may reach completion, the associated diffusional compositional changes may not. This incomplete transformation could result in the formation of nanoscale solute-lean pockets within the β phase matrix. These solute-lean pockets could serve as favorable nucleation sites for subsequent fine scale α precipitation. A similar indirect influence of isothermal ω phase on α precipitation has been observed in cast Ti-5553 alloy during upquench heat treatment [28]. Secondly, there is inevitably absorption of oxygen in the DEDed Ti-5553, arising from the oxygen contamination during solidification even under an inert gas environment or the oxygen from feedstock powder [51,52]. The results from the LECO chemical analysis in the present case, and the 3D APT results (Figs. 6-7 and Table 1) reveal the pickup of oxygen in the DEDed Ti-5553 during the DED process, compared to the powder feedstock. Oxygen, a known characteristic α phase stabilizer, could enhance the driving force for α nucleation [68,69]. Additionally, our recent study using atom probe tomography has shown than the segregation of oxygen at the grain boundary in the cast Ti-5553 plays a critical role responsible for the grain boundary α formation [70]. It is reasonable to consider that oxygen absorbed during DED process potentially contributes to the larger number density of fine-scaled α in the DEDed Ti-5553 at 700°C. To unambiguously identify the role of oxygen and nanoscale ω precipitates on the fine scale α microstructure, the early stages of α precipitation at 700°C are being investigated using TEM and 3D APT. The results will be reported in our future work.

4.2.3. Super-refined α microstructure

After DEDed Ti-5553 is slowly heated to 600°C at 5 °C/min, 0.5 °C/ min, and isothermally held for 2 hours, the so-called super-refined $\boldsymbol{\alpha}$ microstructure with the number densities of $30.2 {\pm} 0.9$ and $47.8 {\pm} 0.8$ ppts/µm² can form. It is hypothesized that during the slow heating, nanostructures, e.g., nanoscale isothermal ω phase and O' phase particles formed in the DEDed Ti-5553, may assist in the formation of superrefined α precipitates. The ω phase assisted α precipitation has been extensively observed in several different cast metastable β -Ti alloys. Li et al. observed that in the Ti-6Cr-5Mo-5 V-4Al (wt%) alloy, oxygen tends to accumulate at the pre-formed ω/β interface, creating a region enriched in oxygen that acts as favorable nucleation sites for subsequent α phase precipitation [26,71]. This enrichment of oxygen facilitates the formation of a large number of very fine-scaled α precipitates through a mixed displacive-diffusional transformation mechanism. Nag et al. reported the solute segregation near the pre-formed ω/β interface in cast Ti-5553 [72]. Unlike oxygen, Al characterized through atom probe tomography segregates at a certain distance from the pre-formed ω/β interface. Al, as an effective α phase stabilizer, can serve as the nucleation sites of α phase formation. Additionally, our recent studies in cast Ti-5553 alloy have revealed that the concentration and stress field near the pre-formed ω/β interface could be modified by the pre-formed ω phase [29]. Both factors can contribute to the resulting formation of super-refined α phase precipitates. Similarly, during the slow heating process in post-heat treatment, DEDed Ti-5553 is maintained at low temperature for sufficient long time to allow athermal ω phase to transform to isothermal ω phase below the ω solvus temperature (~400°C). These isothermal ω phase particles can alter the solute distribution, e.g., the distribution of oxygen and Al, near the ω/β interface and also change the stress field due to the lattice mismatch between the ω phase and β matrix. Thus, the ω phase may create potent nucleation sites for the super-refined α microstructure in DEDed Ti-5553.

It is also worthy to point out that recent studies have suggested the possible influence of O' phase on α nucleation in the Ti-23 Nb-2 O (at%) [50] and Ti-5Al-3Mo-3 V-2Cr-2Zr-1 Nb-1Fe (wt%) alloys [73–75]. Li et al. characterized the segregation of oxygen near the O'/ β interface and claimed such an oxygen enriched zone could act as favorable nucleation sites for α precipitation in metastable β Ti-23 Nb-2 O (at%) alloy [50].

Song et al. suggested that the uniform and dense distribution of fine-scaled α precipitates formed in aged metastable β Ti-5Al-3-Mo-3 V-2Cr-2Zr-1 Nb-1Fe is due to the large number of O' precursors assisted α nucleation [73]. These findings indicate that during the slow heating in the post-heat treatment of DEDed Ti-5553, the nanoscale O' phase particles could potentially play a role in the formation of the super-refined α precipitates. In summary, in our current study, nanoscale ω and O' phase formed during the rapid cooling in the DED process, significantly impacting the local structure and/or composition; therefore, creating more nucleation sites for subsequent super-refined α phase precipitation in the interior of the β grains.

4.3. Influence of α microstructure on mechanical properties

Post-heat treatments result in varied hardness, yield strength, ultimate strength, and ductility of DEDed Ti-5553, which attributed to the formation of α microstructures with different sizescales, as shown in Table 2. The yield strength of metastable β-Ti alloys with a fixed composition is mainly dependent on the number density and distribution of α precipitates, arising from the ability of α precipitates in hindering the dislocation movement [34,35]. The critical resolved shear stress (σ) for a dislocation overcoming α precipitates is inversely proportional to the inter-particle spacing (l), and is expressed as: $\sigma \propto \frac{K}{l}$, where K is the Taylor factor, and l as inter-particle spacing between α precipitates. In this study, the coarse, refined, and super-refined α microstructures, although almost uniformly distributed in the interior of β grains, exhibit distinct number densities, 0.02 ± 0.003 ppts/ μ m² for coarse α microstructure, 10.7 ± 1.1 ppts/ μ m² for refined α microstructure and over 30.2 ± 0.9 ppts/ μ m² for super-refined α microstructure. Thus, the relative higher number density of refined and super-refined α microstructures can contribute to the higher yield strength compared to the coarse α microstructure in the DEDed Ti-5553.

The α precipitates also influence the deformation mechanisms of the metastable β-Ti alloys. For comparison, in case of the Ti-12Mo (wt%) alloy, the dominant effects of twinning induced plasticity (TWIP) and transformation induced plasticity (TRIP) lead to high strain hardening and substantial uniform tensile ductility despite the presence of athermal $\boldsymbol{\omega}$ precipitates within the $\boldsymbol{\beta}$ grains. After a short-time aging at low temperature (~150–200°C), early stages of isothermal ω formation significantly increases the strength without a substantial loss of ductility; while on the other hand, after long-time aging at low temperature, well-developed isothermal ω precipitates, and the more β stabilized matrix suppresses deformation twinning (e.g., {332}<113> type), as well as stress-induced martensitic transformation, thus significantly decreasing the ductility [76,77]. In β-solutionized Ti-5553, novel $\{10\ 9\ 3\}<3\ 3\ 1>$ deformation twins and martensitic α'' phase have been recently identified [78]. In our study, in DEDed Ti-5553, nanoscale ω and O' phases are formed without the presence of any α precipitates. The stress-strain plot for the DEDed Ti-5553, shown in Fig. 14, exhibits relatively high ductility (\sim 19.1 \pm 1.0 % elongation), but no strain-hardening. Therefore, it can be hypothesized that the deformation in case of as-processed Ti-5553 is dominated by dislocation-mediated plasticity. The nanoscale ω and O' phase precipitates do not impede dislocations to any significant degree, leading to the relatively high ductility of DEDed Ti-5553 (\sim 19.1 \pm 1.0 % elongation). Even though solute partitioning has been observed in the nanoscale ω precipitates based on 3D APT results, it represents the early stages of isothermal ω formation. These ω precipitates do not lead to embrittlement and consequently the DEDed Ti-5553 alloy maintains good ductility. However, after different α microstructures are formed in the DEDed Ti-5553 after post-heat treatment, the mean free path for dislocation slip is severely restricted. Additionally, the large number of α/β interfaces will influence the dislocation slip transmission. Dislocations in β matrix are obstructed and pile up at the α/β interfaces, and these semi-coherent interfaces need to transfer the slip by dislocation or twinning inside

the α precipitates. For the relatively coarse α precipitates, internal twinning and dislocation slip could be activated, and thus contribute to the relative higher strength and ductility (yield strength 857.2 \pm 55.4 MPa and elongation 10.4 \pm 1.8 %), while for the refined α precipitates, the larger number of α/β interfaces could significantly increase the strength but substantially decreases the ductility (yield strength 1460.6 \pm 60.0 MPa and 3.6 \pm 5.6 % elongation).

5. Conclusion

This study investigates the microstructure evolution of DEDed metastable β Ti-5553 alloy as affected by post-heat treatments and its effect on material's strength and ductility. Notably, in DEDed Ti-5553, nanoscale isothermal ω phase and O' phase are formed in the coarse columnar β grains without the formation of any α phase precipitates. The post-heat treatments have been demonstrated to effectively induce different fine-scaled α microstructures in DEDed Ti-5553 via different phase transformation mechanisms, affecting the mechanical performance of DEDed Ti-5553, including the hardness, tensile strength, and ductility. Specifically, the key findings are summarized as follows:

In DEDed Ti-5553, nanoscale isothermal ω phase with hexagonal structure and nanoscale O' phase with orthorhombic structure are formed in the coarse columnar β grains without the formation of any diffusional hcp-structured α phase precipitates, resulting in the hardness of 296±5.6 HV, yield strength of 809±75.0 MPa, ultimate strength of 858.3±75.0 MPA, total elongation of ~19.1±1 %, and Young's modulus of 79.1 ± 2.0 GPa.

Up-quenching and isothermally aging at 600° C for 2 hours produces a refined α microstructure with the number density of 10.7 ± 1.1 ppts/ μ m² in DEDed Ti-5553 via pseudospinodal decomposition. The refined α microstructure enhanced the hardness to 406 ± 4.6 HV, yield strength to 1425.5 ± 54.0 MPa, and ultimate strength to 1477.5 ± 49.0 MPa, but the total elongation decreased to approximately 3.7 ±0.1 %.

Up-quenching and isothermally aging at 700°C for 2 hours generates a fine-scaled α microstructure with the number density of 6.2 ± 0.6 ppts/ μm^2 in DEDed Ti-5553, possibly influenced by the combination of multiple factors, including both the indirect influence of nanoscale isothermal ω phase particles formed during DED process and the excess oxygen introduced during DED process. The fine-scaled α microstructure raised the hardness to 368 ± 5.6 HV, yield strength to 1079.4 ± 50.5 MPa, and ultimate strength to 1120.6 ± 63.9 MPa, but reduced the total elongation to 6.6 ± 0.5 %.

Up-quenching and isothermally aging at $800^{\circ}C$ for 2 hours yields a coarse α microstructure with the number density of 6.2 ± 0.6 ppts/ μm^2 in DEDed Ti-5553, via the classical nucleation and growth mechanism. The coarse α microstructure improved the hardness to $332\pm6.6\,$ HV, yield strength to $857.2\pm55.4\,$ MPa, and ultimate strength to $913.6\pm44.1\,$ MPa, and maintained $10.4\pm1.8\,$ % total elongation.

Slow heating up at 5 °C/min followed by isothermally aging at 600 °C for 2 hours leads to a super-refined α microstructure with the number density of 30.2 \pm 0.9 ppts/ μm^2 in DEDed Ti-5553, via the ω phase and O' phase assisted α nucleation mechanism. The super-refined α microstructure increased the hardness to 443 \pm 9.7 HV, yield strength to 1460.6 \pm 60.0 MPa, and ultimate strength to 1534.6 \pm 46.1 MPa but sacrifices the total elongation to only 3.6 \pm 5.6 %.

In conclusion, our study conclusively demonstrates the tunability of DEDed Ti-5553's strength and ductility by the manipulation of α microstructures through different post-heat treatments. This research provides valuable insights into enhancing the mechanical properties of AM-fabricated metastable $\beta\text{-Ti}$ alloys, paving the way for further advancements in material design and processing.

CRediT authorship contribution statement

Yiliang Liao: Writing – review & editing, Supervision, Resources, Conceptualization. Mohammad Merajul Haque: Investigation, Formal analysis. Tirthesh Ingale: Investigation, Formal analysis. Rajarshi Banerjee: Writing – review & editing. Vishal Soni: Writing – review & editing, Investigation, Formal analysis. Yufeng Zheng: Writing – review & editing, Supervision, Resources, Funding acquisition, Conceptualization. Sydney Fields: Writing – review & editing, Investigation, Formal analysis. Dian Li: Writing – original draft, Investigation, Formal analysis, Conceptualization. Deepak Pillai: Writing – review & editing, Investigation, Formal analysis. Xing Zhang: Writing – review & editing, Investigation, Formal analysis.

Declaration of Competing Interest

The authors declare that they have no known competing financial interests or personal relationships that could have appeared to influence the work reported in this paper.

Data availability

Data will be made available on request.

Acknowledgements

DL, SF, DP, and YZ appreciate the financial support from National Science Foundation, grant #2122272 and #2346524. YL thanks the financial support from National Science Foundation, grant #2231078. The authors would also like to thank Sarang Saji for help with the nanoindentation experiments.

Appendix A. Supporting information

Supplementary data associated with this article can be found in the online version at doi:10.1016/j.addma.2024.104436.

References

- D. Banerjee, J.C. Williams, Perspectives on titanium science and technology, Acta Mater. 61 (3) (2013) 844–879, https://doi.org/10.1016/j.actamat.2012.10.043.
- [2] J.D. Cotton, R.D. Briggs, R.R. Boyer, S. Tamirisakandala, P. Russo, N. Shchetnikov, J.C. Fanning, State of the art in beta titanium alloys for airframe applications, Jom 67 (6) (2015) 1281–1303, https://doi.org/10.1007/s11837-015-1442-4.
- [3] J.C. Williams, R.R. Boyer, Opportunities and issues in the application of titanium alloys for aerospace components, Metals 10 (6) (2020) 705, https://doi.org/ 10.3390/met10060705.
- [4] S. Veeck, D. Lee, R. Boyer, R. Briggs, The castability of Ti-5553 alloy: its microstructure and properties, J. Adv. Mater. 37 (4) (2005) 40–45.
- [5] P.-J. Arrazola, A. Garay, L.-M. Iriarte, M. Armendia, S. Marya, F. Le Maître, Machinability of titanium alloys (Ti6Al4V and Ti555. 3), J. Mater. Process. Technol. 209 (5) (2009) 2223–2230, https://doi.org/10.1016/j. matprotec.2008.06.020.
- [6] D. Zhang, D. Qiu, M.A. Gibson, Y. Zheng, H.L. Fraser, D.H. StJohn, M.A. Easton, Additive manufacturing of ultrafine-grained high-strength titanium alloys, Nature 576 (7785) (2019) 91–95, https://doi.org/10.1038/s41586-019-1783-1.
- [7] T. Zhang, Z. Huang, T. Yang, H. Kong, J. Luan, A. Wang, D. Wang, W. Kuo, Y. Wang, C.-T. Liu, In situ design of advanced titanium alloy with concentration modulations by additive manufacturing, Science 374 (6566) (2021) 478–482, https://doi.org/10.1126/science.abj3770.
- [8] Y. Zhu, K. Zhang, Z. Meng, K. Zhang, P. Hodgson, N. Birbilis, M. Weyland, H. L. Fraser, S.C.V. Lim, H. Peng, Ultrastrong nanotwinned titanium alloys through additive manufacturing, Nat. Mater. 21 (11) (2022) 1258–1262, https://doi.org/10.1038/s41563-022-01359-2.
- [9] Z. Liu, B. He, T. Lyu, Y. Zou, A review on additive manufacturing of titanium alloys for aerospace applications: directed energy deposition and beyond Ti-6Al-4V, Jom 73 (2021) 1804–1818, https://doi.org/10.1007/s11837-021-04670-6.
- [10] B.E. Carroll, T.A. Palmer, A.M. Beese, Anisotropic tensile behavior of Ti-6Al-4V components fabricated with directed energy deposition additive manufacturing, Acta Mater. 87 (2015) 309–320, https://doi.org/10.1016/j.actamat.2014.12.054.
- [11] B. Baufeld, O. Van der Biest, R. Gault, Additive manufacturing of Ti-6Al-4V components by shaped metal deposition: microstructure and mechanical properties, Mater. Des. 31 (2010) S106-S111, https://doi.org/10.1016/j.matdes.2009.11.032.

- [12] H. Gong, K. Rafi, H. Gu, T. Starr, B. Stucker, Analysis of defect generation in Ti–6Al–4V parts made using powder bed fusion additive manufacturing processes, Addit. Manuf. 1 (2014) 87–98, https://doi.org/10.1016/j.addma.2014.08.002.
- [13] W. Xu, M. Brandt, S. Sun, J. Elambasseril, Q. Liu, K. Latham, K. Xia, M. Qian, Additive manufacturing of strong and ductile Ti-6Al-4V by selective laser melting via in situ martensite decomposition, Acta Mater. 85 (2015) 74-84, https://doi. org/10.1016/j.actamat.2014.11.028.
- [14] J. Heigel, P. Michaleris, E.W. Reutzel, Thermo-mechanical model development and validation of directed energy deposition additive manufacturing of Ti-6Al-4V, Addit. Manuf. 5 (2015) 9-19, https://doi.org/10.1016/j.addma.2014.10.003.
- [15] A. Azarniya, X.G. Colera, M.J. Mirzaali, S. Sovizi, F. Bartolomeu, W.W. Wits, C. Y. Yap, J. Ahn, G. Miranda, F.S. Silva, Additive manufacturing of Ti–6Al–4V parts through laser metal deposition (LMD): process, microstructure, and mechanical properties, J. Alloy. Compd. 804 (2019) 163–191, https://doi.org/10.1016/j.iallcom.2019.04.255.
- [16] M. Ansari, A. Martinez-Marchese, Y. Huang, E. Toyserkani, A mathematical model of laser directed energy deposition for process mapping and geometry prediction of Ti-5553 single-tracks, Materialia 12 (2020) 100710, https://doi.org/10.1016/j. mtla 2020 100710
- [17] C. Hicks, T. Konkova, P. Blackwell, Influence of laser power and powder feed rate on the microstructure evolution of laser metal deposited Ti-5553 on forged substrates, Mater. Charact. 170 (2020) 110675, https://doi.org/10.1016/j. matchar.2020.110675.
- [18] C. Hicks, G. Sivaswamy, T. Konkova, P. Blackwell, Anisotropic tensile properties and failure mechanism of laser metal deposited Ti-5Al-5Mo-5V-3Cr alloy before and after sub-transus heat-treatment, Mater. Sci. Eng. A 825 (2021) 141928, https://doi.org/10.1016/j.msea.2021.141928.
- [19] D. Sharma, S.R. Kada, D. Fabijanic, D. Parfitt, B. Chen, B. Roebuck, M. E. Fitzpatrick, M.R. Barnett, The ageing response of direct laser deposited metastable β-Ti alloy, Ti–5Al–5Mo–5V–3Cr, Addit. Manuf. 48 (2021) 102384, https://doi.org/10.1016/j.addma.2021.102384.
- [20] Y. Liu, L. Xu, C. Qiu, Development of an additively manufactured metastable beta titanium alloy with a fully equiaxed grain structure and ultrahigh yield strength, Addit. Manuf. 60 (2022) 103208, https://doi.org/10.1016/j.addma.2022.103208.
- [21] H. Schwab, M. Bönisch, L. Giebeler, T. Gustmann, J. Eckert, U. Kühn, Processing of Ti-5553 with improved mechanical properties via an in-situ heat treatment combining selective laser melting and substrate plate heating, Mater. Des. 130 (2017) 83–89, https://doi.org/10.1016/j.matdes.2017.05.010.
- [22] H.D. Carlton, K.D. Klein, J.W. Elmer, Evolution of microstructure and mechanical properties of selective laser melted Ti-5Al-5V-5Mo-3Cr after heat treatments, Sci. Technol. Weld. Join. 24 (5) (2019) 465–473, https://doi.org/10.1080/ 13621718.2019.1594589.
- [23] C. Hicks, T. Konkova, P. Blackwell, MATEC Web of Conferences. Microstructure development in Laser Metal Deposition of Ti-5553, EDP Sciences, 2020, p. 03019, https://doi.org/10.1051/matecconf/202032103019.
- [24] S. Nag, Y. Zheng, R.E.A. Williams, A. Devaraj, A. Boyne, Y. Wang, P.C. Collins, G. B. Viswanathan, J.S. Tiley, B.C. Muddle, R. Banerjee, H.L. Fraser, Non-classical homogeneous precipitation mediated by compositional fluctuations in titanium alloys, Acta Mater. 60 (18) (2012) 6247–6256, https://doi.org/10.1016/j.actamat 2012 07 033
- [25] A. Devaraj, V.V. Joshi, A. Srivastava, S. Manandhar, V. Moxson, V.A. Duz, C. Lavender, A low-cost hierarchical nanostructured beta-titanium alloy with high strength, Nat. Comms. Nat. Commun. 7 (2016) 11176, https://doi.org/10.1038/ ncomms11176.
- [26] T. Li, J.M. Cairney, D. Kent, M.S. Dargusch, D. Kent, G. Sha, The mechanism of omega-assisted alpha phase formation in near beta-Ti alloys, Scr. Mater. 104 (2015) 75–78, https://doi.org/10.1016/j.scriptamat.2015.04.007.
- [27] Y. Zheng, D. Choudhuri, T. Alam, R.E.A. Williams, R. Banerjee, H.L. Fraser, The role of cuboidal ω precipitates on α precipitation in a Ti-20V alloy, Scr. Mater. 123 (2016) 81–85, https://doi.org/10.1016/j.scriptamat.2016.06.004.
- [28] Y. Zheng, R.E.A. Williams, J.M. Sosa, T. Alam, Y. Wang, R. Banerjee, H.L. Fraser, The Indirect influence of the ω phase on the degree of refinement of distributions of the α phase in metastable β-titanium alloys, Acta Mater. 103 (2016) 165–173, https://doi.org/10.1016/j.actamat.2015.09.053.
- [29] Y. Zheng, R.E.A. Williams, D. Wang, R. Shi, S. Nag, P. Kami, J.M. Sosa, R. Banerjee, Y. Wang, H.L. Fraser, The role of ω phase in the formation of extremely refined distributions of α phase in titanium alloys, Acta Mater. 103 (2016) 850–858, https://doi.org/10.1016/j.actamat.2015.11.020.
- [30] A. Boyne, D. Wang, R.P. Shi, Y. Zheng, A. Behera, S. Nag, J.S. Tiley, H.L. Fraser, R. Banerjee, Y. Wang, Pseudospinodal mechanism for fine alpha/beta microstructures in beta-Ti alloys, Acta Mater. 64 (2014) 188–197, https://doi.org/ 10.1016/j.actamat.2013.10.026.
- [31] Y. Wang, M. Hao, D. Li, P. Li, Q. Liang, D. Wang, Y. Zheng, Q. Sun, Y. Wang, Enhanced mechanical properties of Ti-SAl-5Mo-5V-3Cr-1Zr by bimodal lamellar precipitate microstructures via two-step aging, Mater. Sci. Eng. A 829 (2022) 142117, https://doi.org/10.1016/j.msea.2021.142117.
- [32] C.A. Salvador, E.S. Lopes, J. Bettini, R. Caram, Formation of alpha phase via pseudospinodal decomposition in Ti-Nb-Fe based alloys, Mater. Lett. 189 (2017) 201–205, https://doi.org/10.1016/j.matlet.2016.11.097.
- [33] V.C. Opini, C.A.F. Salvador, K.N. Campo, E.S.N. Lopes, R.R. Chaves, R. Caram, a phase precipitation and mechanical properties of Nb-modified Ti-5553 alloy, MSA Mater. Sci. Eng. A 670 (2016) 112–121, https://doi.org/10.1016/j.
- [34] S.A. Mantri, D. Choudhuri, T. Alam, G.B. Viswanathan, J.M. Sosa, H.L. Fraser, R. Banerjee, Tuning the scale of alpha precipitates in beta-titanium alloys for

- achieving high strength, Scr. Mater. 154 (2018) 139–144, https://doi.org/10.1016/j.scriptamat.2018.05.040.
- [35] S.A. Mantri, D. Choudhuri, A. Behra, J.D. Coton, N. Kumar, R. Banerjee, Influence of fine-scale alpha precipitation on the mechanical properties of the beta titanium alloy beta-21S, Matel Mater. Trans. A 46 (7) (2015) 2803–2808, https://doi.org/ 10.1007/s11661-015-2944-y.
- [36] M. Strantza, B. Vrancken, M.B. Prime, C.E. Truman, M. Rombouts, D. Brown, P. Guillaume, D. Van Hemelrijck, Directional and oscillating residual stress on the mesoscale in additively manufactured Ti-6Al-4V, Acta Mater. 168 (2019) 299–308, https://doi.org/10.1016/j.actamat.2019.01.050.
- [37] T. Furuhara, H. Nakamori, T. Maki, Crystallography of α phase precipitated on dislocations and deformation twin boundaries in a β titanium alloy, Mater. Trans. JIM 33 (6) (1992) 585–595, https://doi.org/10.2320/matertrans1989.33.585.
- [38] D. Qiu, R. Shi, D. Zhang, W. Lu, Y. Wang, Variant selection by dislocations during α precipitation in α/β titanium alloys, Acta Mater. 88 (2015) 218–231, https://doi.org/10.1016/j.actamat.2014.12.044.
- [39] J.M. Sosa, D.E. Huber, B. Welk, H.L. Fraser, Development and application of MIPAR™: a novel software package for two-and three-dimensional microstructural characterization, Integr. Mater. Manuf. Innov. 3 (1) (2014) 10, https://doi.org/ 10.1186/2193-9772-3-10.
- [40] N. Ramachandiran, H. Asgari, F. Dibia, R. Eybel, A. Gerlich, E. Toyserkani, Effect of non-lamellar α precipitate morphology on the mechanical properties of Ti5553 parts made by laser powder-bed fusion at high laser scan speeds, Mater. Sci. Eng. A 841 (2022) 143039, https://doi.org/10.1016/j.msea.2022.143039.
- [41] R. Nivas, P. Singh, G. Das, S. Das, S. Kumar, B. Mahato, K. Sivaprasad, M. Ghosh, A comparative study on microstructure and mechanical properties near interface for dissimilar materials during conventional V-groove and narrow gap welding, J. Manuf. Process. 25 (2017) 274–283, https://doi.org/10.1016/j. jmapro.2016.12.004.
- [42] N. Ramachandiran, H. Asgari, F. Dibia, R. Eybel, A. Keshavarzkermani, A. Gerlich, E. Toyserkani, Anisotropic tensile behavior of laser powder-bed fusion made Ti5553 parts, Mater. Sci. Eng. A 865 (2023) 144633, https://doi.org/10.1016/j. msea.2023.144633.
- [43] R. Nivas, G. Das, S. Das, B. Mahato, S. Kumar, K. Sivaprasad, P. Singh, M. Ghosh, Effect of stress relief annealing on microstructure & mechanical properties of welded joints between low alloy carbon steel and stainless steel, Metall. Mater. Trans. A 48 (2017) 230–245, https://doi.org/10.1007/s11661-016-3840-9.
- [44] L. Murr, E. Esquivel, S. Quinones, S. Gaytan, M. Lopez, E. Martinez, F. Medina, D. Hernandez, E. Martinez, J. Martinez, Microstructures and mechanical properties of electron beam-rapid manufactured Ti–6Al–4V biomedical prototypes compared to wrought Ti–6Al–4V, Mater. Charact. 60 (2) (2009) 96–105, https://doi.org/ 10.1016/j.matchar.2008.07.006.
- [45] L. Murr, S. Quinones, S. Gaytan, M. Lopez, A. Rodela, E. Martinez, D. Hernandez, E. Martinez, F. Medina, R. Wicker, Microstructure and mechanical behavior of Ti–6Al–4V produced by rapid-layer manufacturing, for biomedical applications, J. Mech. Behav. Biomed. Mater. 2 (1) (2009) 20–32, https://doi.org/10.1016/j.imbbm.2008.05.004.
- [46] S. Al-Bermani, M. Blackmore, W. Zhang, I. Todd, The origin of microstructural diversity, texture, and mechanical properties in electron beam melted Ti-6Al-4V, Metall. Mater. Trans. a 41 (2010) 3422–3434, https://doi.org/10.1007/s11661-010.0397.x
- [47] Y. Zheng, S. Antonov, Q. Feng, R. Banerjee, D. Banerjee, H.L. Fraser, Shuffle-induced modulated structure and heating-induced ordering in the metastable β-titanium alloy, Ti-5Al-5Mo-5V-3Cr, Scr. Mater. 176 (2020) 7–11, https://doi.org/10.1016/j.scriptamat.2019.09.027.
- [48] Y. Zheng, R.E.A. Williams, S. Nag, R. Banerjee, H.L. Fraser, D. Banerjee, The Effect of alloy composition on instabilities in the β phase of titanium alloys, Scr. Mater. 116 (2016) 49–52, https://doi.org/10.1016/j.scriptamat.2016.01.024.
- [49] Y. Zheng, D. Banerjee, H.L. Fraser, A nano-scale instability in the β phase of dilute Ti-Mo Alloys, Scr. Mater. 116 (2016) 131–134, https://doi.org/10.1016/j. scriptamat.2016.01.044.
- [50] T. Li, M. Lai, A. Kostka, S. Salomon, S. Zhang, C. Somsen, M.S. Dargusch, D. Kent, Composition of the nanosized orthorhombic O' phase and its direct transformation to fine α during ageing in metastable β-Ti alloys, Scr. Mater. 170 (2019) 183–188, https://doi.org/10.1016/j.scriptamat.2019.06.008
- https://doi.org/10.1016/j.scriptamat.2019.06.008.

 [51] C. Iantaffi, C.L.A. Leung, Y. Chen, S. Guan, R.C. Atwood, J. Lertthanasarn, M.-S. Pham, M. Meisnar, T. Rohr, P.D. Lee, Oxidation induced mechanisms during directed energy deposition additive manufactured titanium alloy builds, Addit. Manuf. Lett. 1 (2021) 100022, https://doi.org/10.1016/j.addlet.2021.100022.
- [52] J.N. Rousseau, A. Bois-Brochu, C. Blais, Effect of oxygen content in new and reused powder on microstructural and mechanical properties of Ti6Al4V parts produced by directed energy deposition, Addit. Manuf. 23 (2018) 197–205, https://doi.org/ 10.1016/j.addma.2018.08.011.
- [53] S. Antonov, R. Shi, D. Li, Z. Kloenne, Y. Zheng, H.L. Fraser, D. Raabe, B. Gault, Nucleation and growth of α phase in a metastable β-Titanium Ti-SAI-5Mo-5V-3Cr alloy: influence from the nano-scale, ordered-orthorhombic O "phase and α compositional evolution, Scr. Mater. 194 (2020) 113672, https://doi.org/ 10.1016/j.scriptamat.2020.113672.
- [54] R. Shi, D. Li, S. Antonov, X. Liu, Y. Zheng, Origin of morphological variation of grain boundary precipitates in titanium alloys, Scr. Mater. 214 (2022) 114651, https://doi.org/10.1016/j.scriptamat.2022.114651.
- [55] Y. Zheng, R.E.A. Williams, G.B. Viswanathan, W.A.T. Clark, H.L. Fraser, Determination of the structure of α - β interfaces in metastable β -Ti alloys, Acta Mater. 150 (2018) 25–39, https://doi.org/10.1016/j.actamat.2018.03.003.

- [56] H. Schwab, F. Palm, U. Kühn, J. Eckert, Microstructure and mechanical properties of the near-beta titanium alloy Ti-5553 processed by selective laser melting, Mater. Des. 105 (2016) 75–80, https://doi.org/10.1016/j.matdes.2016.04.103.
- [57] M. Wu, M. Linne, J.-B. Forien, N.R. Barton, J. Ye, K. Hazeli, A. Perron, K. Bertsch, Y.M. Wang, T. Voisin, Additively manufactured β-Ti5553 with laser powder bed fusion: Microstructures and mechanical properties of bulk and lattice parts, J. Mater. Process. Technol. 327 (2024) 118354 https://doi.10.1016/j.jmatprotec.2024.118354.
- [58] E. Pang, E. Pickering, S.-I. Baik, D.N. Seidman, N.G. Jones, The effect of zirconium on the omega phase in Ti-24Nb-[0–8] Zr (at%) alloys, Acta Mater. 153 (2018) 62–70, https://doi.org/10.1016/j.actamat.2018.04.016.
- [59] M. Li, X. Min, K. Yao, F. Ye, Novel insight into the formation of α "-martensite and ω-phase with cluster structure in metastable Ti-Mo alloys, Acta Mater. 164 (2019) 322–333, https://doi.org/10.1016/j.actamat.2018.10.048.
- [60] A. Devaraj, S. Nag, R. Srinivasan, R.E.A. Williams, S. Banerjee, R. Banerjee, H. L. Fraser, Experimental evidence of concurrent compositional and structural instabilities leading to omega precipitation in titanium-molybdenum alloys, Acta Mater. 60 (2) (2012) 596–609, https://doi.org/10.1016/j.actamat.2011.10.008.
- [61] S. Nag, A. Devaraj, R. Srinivasan, R.E.A. Williams, N. Gupta, G.B. Viswanathan, J. S. Tiley, S. Banerjee, S.G. Srinivasan, H.L. Fraser, R. Banerjee, Novel mixed-mode phase transition involving a composition-dependent displacive component, Phys. Rev. Lett. 106 (24) (2011) 245701, https://doi.org/10.1103/PhysRevLett.106.245701.
- [62] Q. Liang, Y. Zheng, D. Wang, Y. Hao, R. Yang, Y. Wang, H.L. Fraser, Nano-scale structural non-uniformities in gum like Ti-24Nb-4Zr-8Sn metastable β-Ti alloy, Scr. Mater. 158 (2019) 95–99, https://doi.org/10.1016/j.scriptamat.2018.08.043.
- [63] Q. Liang, D. Wang, Y. Zheng, S. Zhao, Y. Gao, Y. Hao, R. Yang, D. Banerjee, H. L. Fraser, Y. Wang, Shuffle-nanodomain regulated strain glass transition in Ti-24Nb-4Zr-8Sn alloy, Acta Mater. 186 (2020) 415–424, https://doi.org/10.1016/j.scriptamat.2018.08.043.
- [64] Y. Zheng, R. Banerjee, Y. Wang, H. Fraser, D. Banerjee, Pathways to titanium martensite, Trans. Indian Inst. Met. 75 (4) (2022) 1051–1068, https://doi.org/ 10.1007/s12666-022-02559-9.
- [65] D.-G. Ahn, Directed energy deposition (DED) process: state of the art, Int. J. Precis. Eng. Manuf. -Green. Technol. 8 (2021) 703–742, https://doi.org/10.1007/s40684-021-00401-z.
- [66] Y. Zheng, R.E.A. Williams, H.L. Fraser, Characterization of a previously unidentified ordered orthorhombic metastable phase in Ti-5Al-5Mo-5V-3Cr, Scr. Mater. 113 (2016) 202–205, https://doi.org/10.1016/j.scriptamat.2015.10.037.
- [67] P. Narayana, S. Lee, S.-W. Choi, C.-L. Li, C.H. Park, J.-T. Yeom, N. Reddy, J.-K. Hong, Microstructural response of β-stabilized Ti-6Al-4V manufactured by direct energy deposition, J. Alloy. Compd. 811 (2019) 152021, https://doi.org/ 10.1016/j.jallcom.2019.152021.

- [68] K. Chou, E.A. Marquis, Oxygen effects on ω and α phase transformations in a metastable β Ti–Nb alloy, Acta Mater. 181 (2019) 367–376, https://doi.org/ 10.1016/j.actamat.2019.09.049.
- [69] K. Chou, E.A. Marquis, Role of oxygen on the precipitation and deformation behavior of an aged β Ti-15Mo alloy, J. Alloy. Compd. 891 (2022) 161811, https:// doi.org/10.1016/j.jallcom.2021.161811.
- [70] T.S. Prithiv, Z. Kloenne, D. Li, R. Shi, Y. Zheng, H.L. Fraser, B. Gault, S. Antonov, Grain boundary segregation and its implications regarding the formation of the grain boundary α phase in the metastable β-Titanium Ti-5Al-5Mo-5V-3Cr alloy, Scr. Mater. 207 (2022) 114320, https://doi.org/10.1016/j.scriptamat.2021.114320.
- [71] T. Li, D. Kent, G. Sha, L.T. Stephenson, A.V. Ceguerra, S.P. Ringer, M.S. Dargusch, J.M. Cairney, New insights into the phase transformations to isothermal ω and ω-assisted α in near β-Ti alloys, AM Acta Mater. 106 (2016) 353–366, https://doi.org/10.1016/j.actamat.2015.12.046.
- [72] S. Nag, R. Banerjee, R. Srinivasan, J.Y. Hwang, M. Harper, H.L. Fraser, Omegaassisted nucleation and growth of alpha precipitates in the Ti-5Al-5Mo-5V-3Cr-0.5Fe beta titanium alloy, Acta Mater. 57 (7) (2009) 2136–2147, https://doi.org/ 10.1016/j.actamat.2009.01.007.
- [73] B. Song, W. Xiao, C. Ma, L. Zhou, Tuning the strength and ductility of near β titanium alloy Ti-5321 by ω and O' intermediate phases via low-temperature aging, Mater. Sci. Eng. A 855 (2022) 143919, https://doi.org/10.1016/j.msea 2022 143919
- [74] B. Song, W. Xiao, Y. Fu, C. Ma, L. Zhou, Role of nanosized intermediate phases on α precipitation in a high-strength near β titanium alloy, Mater. Lett. (2020) 128147, https://doi.org/10.1016/j.matlet.2020.128147.
- [75] B. Song, Y. Chen, W. Xiao, L. Zhou, C. Ma, Formation of intermediate phases and their influences on the microstructure of high strength near-β titanium alloy, Mater. Sci. Eng. A 793 (2020) 139886, https://doi.org/10.1016/j. matlet.2020.128147.
- [76] S.A. Mantri, F. Sun, D. Choudhuri, T. Alam, B. Gwalani, F. Prima, R. Banerjee, Deformation induced hierarchical twinning coupled with omega transformation in a metastable β-ti alloy, Sci. Rep. 9 (1) (2019) 1–8, https://doi.org/10.1038/ s41598-018-37865-0.
- [77] F. Sun, J.Y. Zhang, P. Vermaut, D. Choudhuri, T. Alam, S.A. Mantri, P. Svec, T. Gloriant, P.J. Jacques, R. Banerjee, F. Prima, Strengthening strategy for a ductile metastable b-titanium alloy using low-temperature aging, Mater. Res. Lett. 5 (8) (2017) 547–553. https://doi.org/10.1038/s41598-018-37865-0.
- [78] S. Antonov, Z. Kloenne, Y. Gao, D. Wang, Q. Feng, Y. Wang, H.L. Fraser, Y. Zheng, Novel deformation twinning system in a cold rolled high-strength metastable-β Ti-5Al-5V–5Mo-3Cr-0.5Fe alloy, Materialia 9 (2020) 100614, https://doi.org/ 10.1038/s41598-018-37865-0.